The Main Himalayan Thrust beneath Nepal and Southern Tibet illuminated by seismic ambient noise and teleseismic P wave coda autocorrelation

Hari Ram Thapa[1], Surya Pachhai[2], Abdelkrim Aoudia[3], Daniel Manu-marfo[3], Keith F. Priestley[4], and Supriyo Mitra[5]

[1]The Abdus Salam International Center for Theoretical Physics (ICTP)
[2]University of Utah
[3]International Centre for Theoretical Physics
[4]University of Cambridge
[5]Indian Institute of Science Education and Research Kolkata

January 10, 2023

Abstract

Nepal is an actively deforming region due to its tectonic setting that hosts many destructive earthquakes including the recent 2015 Mw 7.8 Gorkha earthquake. To better understand the physics of earthquakes and their precise location as well as monitoring of seismicity and real-time seismic hazard in the region, a highly resolved 3-D structure of the crust is essential. This study presents a new 3-D S-wave velocity structure of the crust using ambient noise tomography (ANT). This study further constrains the discontinuities beneath Himalaya Nepal using teleseismic P-wave coda autocorrelation. The results from the P-wave coda autocorrelation identify major seismic discontinuities in the crust including the Main Himalayan Thrust (MHT). The MHT with two ramps correlates well with a low S-wave velocity layer obtained from the ANT. The first ramp agrees with the duplex structure in the MHT beneath Lesser Himalaya while the second connects flat low velocity beneath High Himalaya to a broad low-velocity zone beneath South Tibet. The geometry and extent of the High Himalaya low-velocity layer mimics the decollement coupling zone inferred from GPS data with widths of 50-70 km north of the nucleation of the 2015 Mw 7.8 Gorkha earthquake and 90-100 km north of the source of the Mw 8.4 1934 earthquake. The occurrence of millenary Mw>9.0 earthquakes in Central and Eastern Nepal would require either a wider coupling low velocity zone compared to the ones identified in this work or the involvement of southernmost Tibet low velocity decoupling zone so to store enough elastic energy.

Hosted file

951441_0_art_file_10558543_rn33pj.docx available at https://authorea.com/users/569571/articles/615358-the-main-himalayan-thrust-beneath-nepal-and-southern-tibet-illuminated-by-seismic-ambient-noise-and-teleseismic-p-wave-coda-autocorrelation

Hosted file

951441_0_supp_10558569_rnxjfv.docx available at https://authorea.com/users/569571/articles/615358-the-main-himalayan-thrust-beneath-nepal-and-southern-tibet-illuminated-by-seismic-ambient-noise-and-teleseismic-p-wave-coda-autocorrelation

The Main Himalayan Thrust beneath Nepal and Southern Tibet illuminated by seismic ambient noise and teleseismic P wave coda autocorrelation

Hari Ram Thapa[1-2](hthapa@ictp.it), Surya Pachhai[3], Abdelkrim Aoudia[1], Daniel Manu-Marfo[1], Keith Priestley[4], and Supriyo Mitra[5]

1. *The Abdus Salam International Center for Theoretical Physics, Trieste, Italy*
2. *University of Trieste, Piazzale Europa, 1, 34127 Trieste TS*
3. *Department of Geology and Geophysics, University of Utah, 115 S 1460 E, Salt Lake City, UT 84112*
4. *University of Cambridge, The Old Schools, Trinity Ln, Cambridge CB2 1TN, United Kingdom*
5. *India Institute of Science Education and Research (IISER) Kolkata, India*

Key points:

1. Main Himalayan Thrust (MHT) as a system of low-velocity zones connected by ramps and duplex structure present in MHT beneath Lesser Himalaya.
2. Presence of mid crustal low velocity reservoir beneath High Himalaya and South Tibet.
3. Presence of low velocity on MHT surface at north of Kathmandu and east of rupture of 2015 Gorkha earthquake.

Abstract

Nepal is an actively deforming region due to its tectonic setting that hosts many destructive earthquakes including the recent 2015 Mw 7.8 Gorkha earthquake. To better understand the physics of earthquakes and their precise location as well as monitoring of seismicity and real-time seismic hazard in the region, a highly resolved 3-D structure of the crust is essential. This study presents a new 3-D S-wave velocity structure of the crust using ambient noise tomography (ANT). This study further constrains the discontinuities beneath Himalaya Nepal using teleseismic P-wave coda autocorrelation. The results from the P-wave coda autocorrelation identify major seismic discontinuities in the crust including the Main Himalayan Thrust (MHT). The MHT with two ramps correlates well with a low S-wave velocity layer obtained from the ANT. The first ramp agrees with the duplex structure in the MHT beneath Lesser Himalaya while the second connects flat low velocity beneath High Himalaya to a broad low-velocity zone beneath South Tibet. The geometry and extent of the High Himalaya low-velocity layer mimics the decollement coupling zone inferred from GPS data with widths of 50-70 km north of the nucleation of the 2015 Mw 7.8 Gorkha earthquake and 90-100 km north of the source of the Mw 8.4 1934 earthquake. The occurrence of millenary Mw>9.0 earthquakes in Central and Eastern Nepal would require either a wider coupling low velocity zone compared to the ones identified in this work or the involvement of southernmost Tibet low velocity decoupling zone so to store enough elastic energy.

Keywords: Himalaya Nepal, Ambient Noise, Bayesian Inversion, 3-D Shear Wave Structure, Crustal Discontinuities, Mid-crustal Low Velocity, Ramps, Duplex Structure, Earthquake Hazard

Plain Language Summary

Nepal is located near the plate boundaries between the Indian and Eurasian plates, resulting in damaging earthquakes in the region. However, we do not know exactly what controls the earthquake processes beneath Himalaya Nepal due to its complex geological settings and lack of detailed seismic properties beneath this region. Here we present the detailed S-wave velocity image up to 60-km depth beneath Himalaya Nepal that shows how fast/slow the S-wave propagates, relating to the material properties in the crust beneath Himalaya. We used the data extracted from the recordings of noise coming from, for example, traffic, ocean, and atmosphere. We also utilized the data that are sensitive to the sharp transition of material properties. The estimated S-wave velocity near the surface is consistent with the material found on the surface of the crust. In this study, we show that the Main Himalayan Thrust can be described as a system of low-velocity zones connected by ramps. In particular the low-velocity layer identified beneath the High Himalaya in Central and Eastern Nepal mimics the interseismic coupling zone inferred from GPS data. A systematic mapping of this layer beneath all the Himalaya may allow a better understanding of the earthquake hazard.

1. Introduction

The continental collision between India and Asia initiated ~50 to 70 million years ago (e.g., DeCelles et al., 2014; Molnar, 1984; Molnar & Tapponnier, 1975; Tapponnier et al., 1982) due to the closing of the Tethys Sea and resulted in the formation of the Himalayan range. The convergence rate of these plates reached its maximum of ~16 cm/year in the initial stage of collision and decreased rapidly after the collision followed by a steady rate of ~5 cm/year (Figure 1a, e.g., Copley et al., 2010; Molnar & Tapponnier, 1975). The closure of the Tethys Sea formed the Indus-Yarlung suture (IYS) zone between the northernmost part of the Himalayas and southern Tibet (orange line in Figure 1a; Dewey & Bird, 1970; Searle et al., 1987). Additionally, the Himalayan crust consists of a series of parallel and in-sequence thrust faults dipping towards the north. These faults are Main Frontal Thrust (MFT), Main Boundary Thrust (MBT), and Main Central Thrust (MCT) (Figure 1a, e.g., Gansser, 1964; Meigs et al., 1995; Hodges, 2000) from the south to the north. They divide the crust into three lithotectonic units in the east-west direction. The MFT separates the Himalayan foreland sedimentary basin in the south from the sub-Himalaya in the north. The MBT bounds the Lesser Himalayas in the north, while the MCT marks the boundary between greater Himalaya in the north and the Lesser Himalayas in the south. The Southern Tibetan Detachment (STD) separates the greater Himalayas from the Tethyan Himalayas to the north. These faults dip northward and meet the Main Himalayan Thrust (MHT) along which Indian lithosphere underthrusts beneath Himalaya. This line of thrust is also known as decollement (Seeber & Armbruster, 1981).

GPS measurements show that MHT is fully locked in the south and accommodates most of the deformation while it is fully unlocked in the north of the interseismic decoupling zone (e.g., Avouac et al., 2015; Bilham et al., 2017) delimited by red dashed lines in Figure 1a) where strain is accumulating (e.g., Ader et al., 2012; Castaldo et al., 2017; Dal Zilio et al., 2021; Lavé & Avouac, 2000). Accordingly, most of the damaging earthquakes in the region happen along the MHT, including the 2015 Gorkha earthquake of M_w 7.8 (e.g., Ader et al., 2012; Avouac et al., 2015; Sapkota et al., 2013). Several past studies investigated the geometry of MHT beneath Himalaya Nepal using structural geology (e.g., Avouac, 2007; Hubbard et al., 2016; Pearson & DeCelles, 2005; Khanal & Robinson, 2013; Pearson, 2002), electromagnetic data (Lemonnier et al., 1999), receiver functions (e.g., Hetényi et al., 2006; Duputel et al., 2016; Nábělek et al., 2009; Schulte-Pelkum et al., 2005; Subedi et al., 2018; Wang et al., 2017), seismicity (e.g., Pandey et al., 1995), thermochronological and thermobarometric data

(Herman et al., 2010), and geodetic data (e.g., Elliott et al., 2016; Mencin et al., 2016). Most of these studies suggest that the MHT has double ramps separated by a flat segment beneath the Lesser Himalayas. However, there are inconsistencies between the dimensions, depths, and dip of the ramps at different locations of the MHT (Figure 1c). There are also controversies on the presence of the mid-crustal ramp in the MHT beneath the frontal part of the High Himalayas (Bollinger et al., 2004; Elliott et al., 2016; Wang et al., 2017; Wobus et al., 2005).

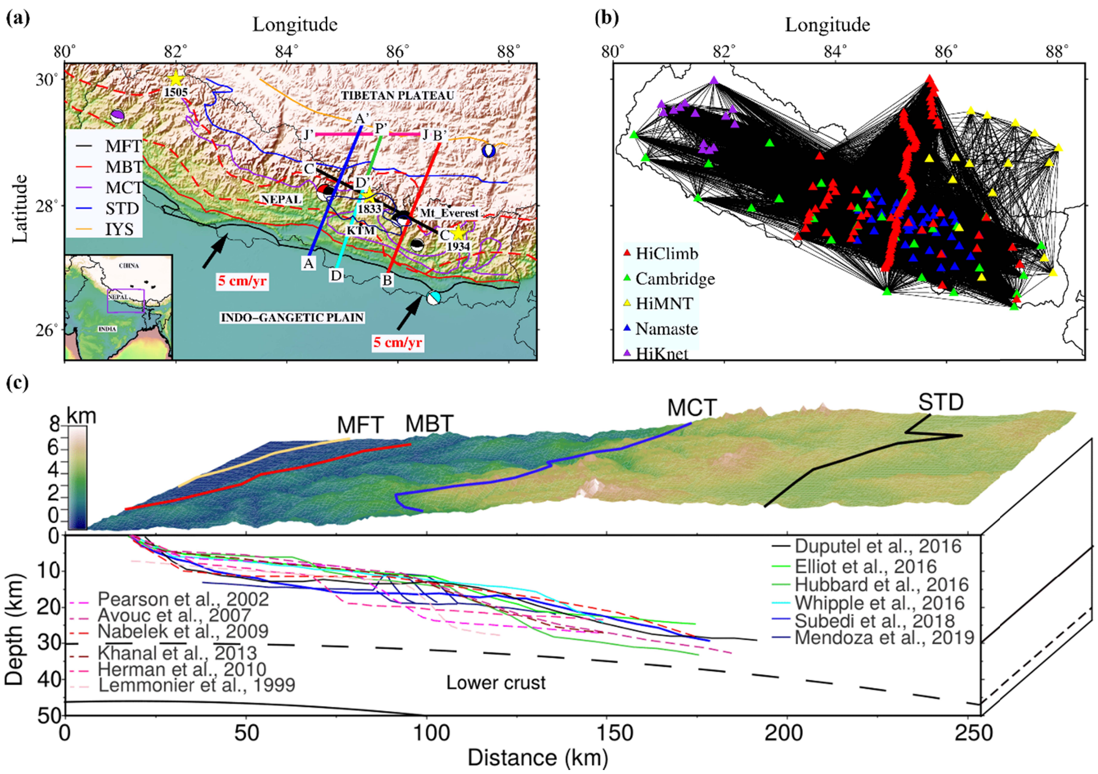

Figure 1. (a) Topographic map of our study area with major thrust faults (MFT, MBT, and MCT), and a normal fault (STD). The colored beach balls indicate earthquakes after 1976 with magnitudes greater than 6 obtained from the Global CMT catalog (Dziewonski et al., 1981; Ekström et al., 2012). Red dashed lines bound an interseismic decoupling zone from 0.9 to 0 coupling (Stevens & Avouac, 2015). b) Ray-coverage using seismic stations from all the networks (represented by different color triangles) considered in this study. (c) The depth and geometry of MHT proposed by previous studies with the topographic map on top.

Although numerous studies focused on the geometry of the MHT in the region, it is not clear why some of the large earthquakes (e.g., 2015 Gorkha earthquake) do not rupture MHT to the surface (e.g., Avouac et al., 2015; Elliott et al., 2016; Grandin et al., 2015; Mencin et al., 2016). It is also unclear why the rupture of the Gorkha earthquake propagated eastward from the hypocenter. Moreover, some of these studies show that the strain transferred to the southern edge of the Gorkha earthquake has not been released by the afterslip process. Further, previous studies showed the high slip potential in the Himalaya region (e.g., Bilham & Wallace, 2005; Stevens & Avouac, 2016). This indicates the potential for future major earthquakes in the Himalayas.

Few studies have provided the lateral variation of compressional P-wave velocity on the MHT surface (e.g., Bai et al., 2016; Pei et al., 2016), however, the details within the rupture area of the 2015 Gorkha earthquake are lacking. Additionally, the precise location or relocation of earthquakes in this region is challenging due to the lack of highly resolved velocity models. This place a limitation on the use of seismicity to map the geometry of MHT (e.g., Kumar et al., 2017; Wang et al., 2017). Hence, a detailed 3-D crustal velocity structure, including the geometry of the MHT and other discontinuities beneath Himalaya Nepal, is crucial to improve our understanding of earthquake processes and seismic hazards in the region.

The wider Himalayan region has been extensively studied using earthquake-based tomography, ambient noise tomography, and/or receiver functions (Agrawal et al., 2021; Hazarika et al., 2020; Kumar et al., 2019; Wei et al., 2021; Wu et al., 2021). However, only limited studies focused on the lithospheric structure beneath Nepal (e.g., Guo et al., 2009; Monsalve et al., 2008), and their lateral resolution is poor. In addition to velocity structure, seismic discontinuities in the crust and upper mantle beneath Himalaya Nepal have been studied mostly using receiver functions (e.g., Nábělek et al., 2009; Nelson et al., 1996; Priestley et al., 2019; Schulte-Pelkum et al., 2005; Xu et al., 2013). Recently, Ruigrok & Wapenaar, (2012) focused on the study of the crustal interfaces beneath Tibet using autocorrelation of global phases. The autocorrelation approach has become a powerful tool for mapping crustal and upper mantle discontinuities (Kennett, 2015) as it provides additional information on the P velocity (Pham & Tkalcic, 2017, 2018) in comparison to S velocity obtained from the receiver functions.

Here, we use ambient noise data from six network stations covering most of Nepal (Figure 1b) to estimate the group and phase velocity maps. We then apply a fully non-linear Bayesian inversion of group and phase velocity dispersions (e.g., Manu-Marfo et al., 2019) to image the 3-D S-wave velocity structure beneath Nepal. This approach provides robust estimates of S-wave velocity and its uncertainty as a function of depth. However, it is challenging to identify the exact depths of crustal discontinuities using group and phase dispersion data. This is because surface wave dispersion data are sensitive to average velocity structure, but they are weakly sensitive to seismic discontinuities (Figure S1). Therefore, uncertainties for S-wave velocity become large at discontinuities. To identify the depth-interface locations, we further apply the P-wave coda autocorrelation approach (Pham & Tkalcic, 2017, 2018). In this paper, we image the geometry of the MHT as it extends from a shallow depth beneath Nepal to the mid-crust under southern Tibet. We interpret our results in terms of structural and geological features as well as earthquake and rupture processes of the 2015 Gorkha earthquake. We integrate our results with recent GPS data (e.g., Lindsey et al., 2018; Mencin et al., 2016; Stevens & Avouac, 2016, 2015) and historical (e.g., Bilham, 2019) as well as paleoseismological data (e.g., Kumar et al., 2001, 2006; Sapkota et al., 2013; Wesnousky et al., 1999, 2018) and discuss the mechanics of the MHT and it seismogenic potential.

2. Data collection and pre-processing

In this study, we used continuous time-series data recorded by five networks in Nepal: Hi-MNT (Sheehan, 2001), Hi-CLIMB (Nabelek, 2002), Namaste (Karplus et al., 2020), HiK-NET (Bollinger et al., 2011), and Cambridge (Priestley et al., 2019). We also added the data from five seismic stations located near the border of India and Nepal that belong to the Indian Institute of Science Education and Research (IISER-K), Kolkata. The Hi-CLIMB stations were operated from 2002 to 2005 while Hi-MNT was installed from 2000 to 2002. The Namaste, Cambridge, and IISER-K networks were operated from 2015 to 2016 just after the 2015 Gorkha earthquake. The HiK-NET was operated from 2014 to 2016, and the data were obtained from RESEIF seismological data portal. In total, we have more than 185 stations providing an unprecedented dense ray coverage (Figure 1b) that enables us to achieve the best lateral resolution in the region so far.

We followed the procedure of Bensen et al. (2007) to compute the cross-correlations between stations. In the pre-processing stage, we cut continuous data into 1-hour lengths. We then removed the mean, trend, and instrument response and filtered the data between 0.02 and 0.33 Hz frequency band. To remove the earthquake signals from the data, we applied one-bit normalization to the filtered data. Finally, we applied spectral whitening. Then we cross-correlated whitened time series recorded by stations at the same time to avoid any effect of the different distribution of the noise source in the time scale. We preferred hourly-long time series for cross-correlation so that a high signal-to-noise ratio (SNR) is achieved, particularly for stations with recordings for a shorter duration. We linearly stacked all cross-correlations obtained for specific station pairs to improve the

SNR by canceling the incoherent noise. Here, we considered cross-correlations with SNR greater than or equal to 10. Examples of linearly stacked cross-correlations for three networks as a function of interstation distance are shown in Figure 2.

For autocorrelation of the P-wave coda, we downloaded the P-wave data for earthquakes of Mw > 5.5 in the epicentral range 30^0 - 95^0 from IRIS, recorded by Hi-CLIMB stations (Nabelek, 2002). We selected this range because the P phase is well separated from other phases. For epicentral distances greater than 95^0, it is difficult to separate the coda of the P wave from the PcP waves. We considered 25 s before and 200 s after the P arrival on the vertical component and rotated the horizontal components into radial and transverse components. We selected the data by visual inspection of both radial and vertical seismograms with high SNR for the P waveform. Vertical component seismograms were selected more than radial components as the P wave is well observed in the vertical component, particularly for teleseismic events. We removed the mean, and trend from the data and applied the taper. We applied three different frequency bands to identify the interfaces: (1) 0.5-4.0 Hz for the shallowest crustal interface, (2) 0.5-2.0 Hz for the mid-crustal interface, and (3) 0.15-1.0 Hz for the Moho.

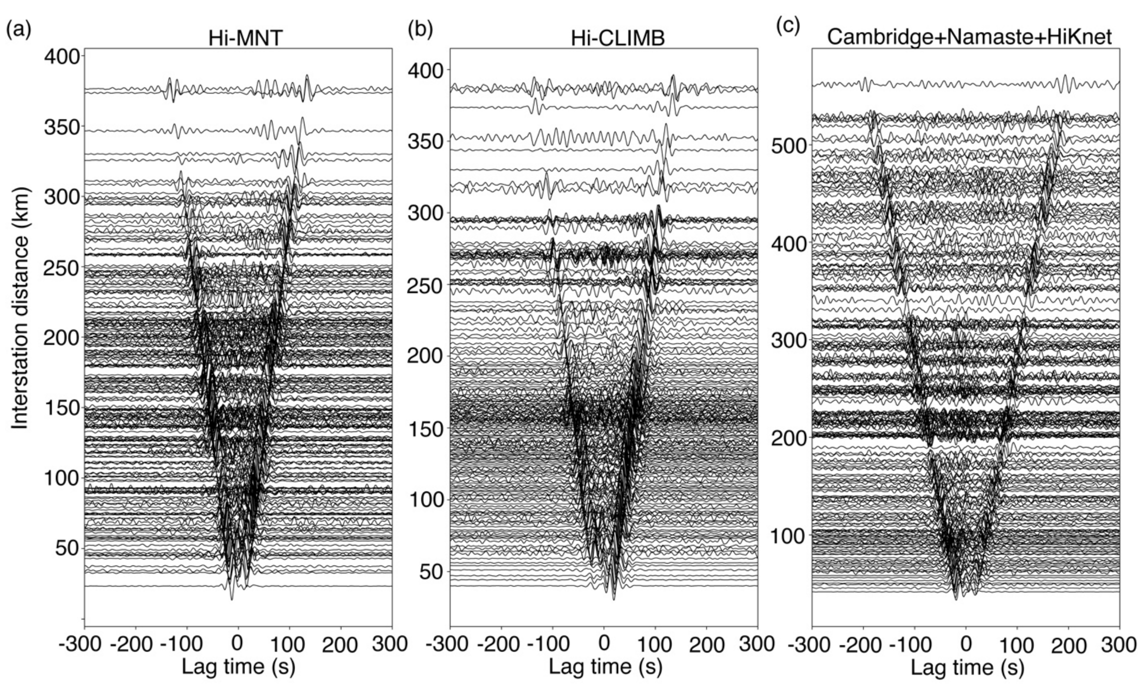

Figure 2. Stacked cross-correlation of all possible pairs that have at least 2 months data in common with another station in the pair, after applying a bandpass filter in the period band 10-40 s for (a) Hi-MNT, (b) Hi-CLIMB, and (c) Cambridge, Namaste, and HiKnet combined.

3. Methodology

3.1 Inversion of ambient noise data

We apply a two-step inversion approach to estimate the S-wave velocity structure from the ambient noise cross-correlations. In the first step, we compute the group and phase tomography maps for periods ranging from 3 to 35 s using the group and phase dispersions between station pairs. The group and phase dispersions across each station pair are measured from the cross-correlograms (Figure 2) by applying Multiple-Filter-Technique (MFT) (Herrmann, 2013). We manually picked all the dispersions and visually inspected them to select the dispersion curves for tomographic inversions. Figure S2 shows an example selection of dispersion curves. Our dispersion curves show variation along different paths between station pairs with low uncertainties (Figure 3). This variation is due to the underlying velocity structures across the ray paths. In Figure 3, average dispersion curves are computed from the stack of all the cross-correlograms while the uncertainties are computed as a standard deviation of dispersions computed for 3 months stack with an overlap of 2 months.

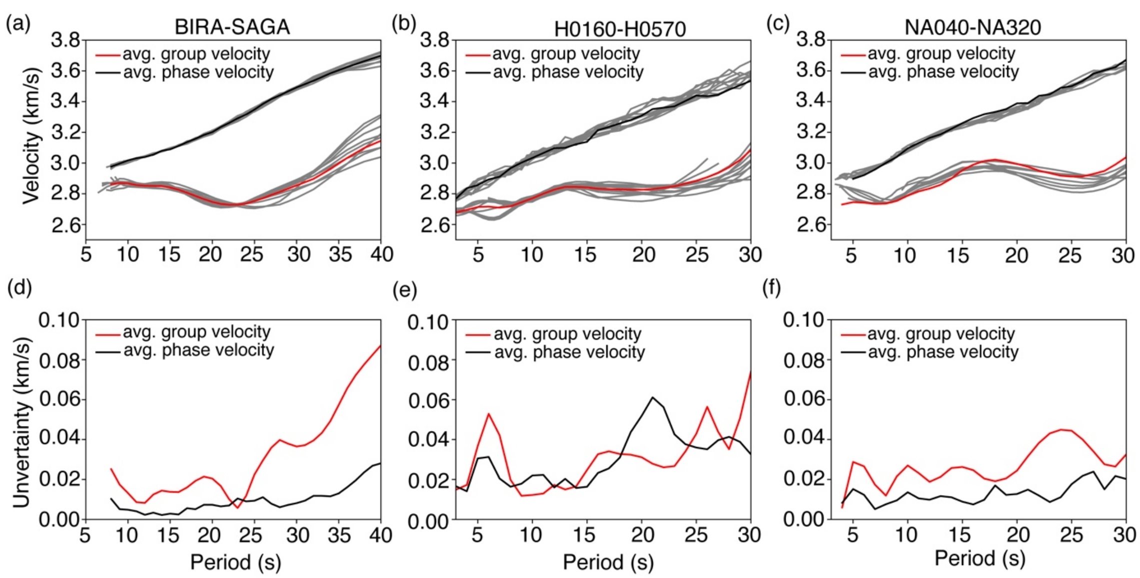

Figure 3. Group (red line) and phase (black line) dispersion curves obtained from the linear stack of all the available data overlain on the 3 months stack with an overlap of 2 months (gray color) for the station pairs: (a) BIRA-SAGA, (b) H0160-H0570, and (c) NA040-NA320. Uncertainty in group and phase dispersion plotted as a function of the period for the station pairs: (d) BIRA-SAGA, (e) H0160-H0570, and (f) NA040-NA320.

This study applies the surface wave tomographic method of Yanovskaya & Ditmar (1990). This method is based on the ray approximation and is a 2-D generalization of the classical 1-D method (Backus & Gilbert, 1968). This method also allows to compute the resolution lengths for the given path (see Text S2).

3.2 Bayesian inversion of dispersion curves

To compute the S-wave velocity as a function of depth, we apply a fully nonlinear Bayesian inversion method (e.g., MacKay, 2003; Mosegaard & Tarantola, 1995), which does not require any regularization, and the number of model parameters remains unknown in the inversion. The same algorithm has been previously applied to study the crust and mantle structure as well as deep Earth structure (Dettmer & Dosso, 2012; Manu-Marfo et al., 2019; Mohammadi et al., 2022; Pachhai et al., 2015, 2022). In this approach, the answer to the inverse problem is expressed in terms of the posterior probability density (PPD), which is proportional to the prior information (independent from the data) and the likelihood, which incorporates data information.

$$p(\boldsymbol{m}|\boldsymbol{d}) \propto p(\boldsymbol{d},\boldsymbol{m})p(\boldsymbol{m}), \qquad (1)$$

where $p(\boldsymbol{m}|\boldsymbol{d})$ represents the PPD and indicates the probability of the model parameters ($\boldsymbol{m}$, which includes number of layers, layer thickness, and S-wave velocity) for given observed data ($\boldsymbol{d}$), $p(\boldsymbol{d},\boldsymbol{m})$ represents the likelihood, which is the probability of data for given model parameters, and $p(\boldsymbol{m})$ represents the prior probability of the model parameters. As the data is fixed, the likelihood function becomes the function of only model parameters, i.e., $L(\boldsymbol{m})$.

The data errors are generally not known and are estimated as a difference between the measured and predicted data. Here, we assume that the data noise has the Gaussian form, therefore, the likelihood function is expressed in the form of L2-norm.

$$L(\boldsymbol{m}) = \frac{1}{|\boldsymbol{C}_d|} exp\left[-|\boldsymbol{d}^{obs} - \boldsymbol{d}(\boldsymbol{m})| \frac{1}{\boldsymbol{C}_{\boldsymbol{d}_{\boldsymbol{i}}}} |\boldsymbol{d}^{obs} - \boldsymbol{d}(\boldsymbol{m})|\right], \qquad (2)$$

where $\boldsymbol{C}_d$ is the noise covariance matrix that includes correlated and uncorrelated noise. Here, our goal is to invert for both group and phase velocity dispersions, therefore, this expression can be modified as:

$$L(\boldsymbol{m}) = \prod_{i=1}^{2} \frac{1}{\left|\boldsymbol{C}_{d_i}\right|} exp\left[-\left|\boldsymbol{d}_i^{obs} - \boldsymbol{d}_i(\boldsymbol{m})\right| \frac{1}{\boldsymbol{C}_{\boldsymbol{d}_{\boldsymbol{i}}}} \left|\boldsymbol{d}_i^{obs} - \boldsymbol{d}_i(\boldsymbol{m})\right| \quad \right], \qquad (3)$$

where 2 is the number of dispersion curves (i.e., one for group and the other for phase velocity) used in the inversion.

For group and phase velocity dispersion curves, the data error can be highly correlated due to various data processing steps. Here, we apply an autoregressive process of order 1 (AR1) model to account the correlated errors. More details of this type of noise model can be found in Dettmer et al. (2012). In this case, the likelihood function can be expressed in the following form.

$$L(\boldsymbol{m}) = \prod_i^2 \frac{1}{\sigma^{npts_i}\sqrt{(2\pi)^{npts_i}}} exp\left[\frac{1}{2\sigma_i^2}\left|\left(\boldsymbol{d}_i^{obs} - \boldsymbol{d}_i(\boldsymbol{m}) - \boldsymbol{d}_i(a_i)\right)\right|^2\right], \qquad (4)$$

where *npts* is the number of data points, $\boldsymbol{d}^{obs}$ is the observed data, $\boldsymbol{d}(\boldsymbol{m})$ is the synthetic prediction, σ is the noise standard deviation, and $\boldsymbol{d}(a)$ is AR1 predictions for AR1 parameter a. In our case, we have two values for the standard deviation of noise and two values for the AR1 parameters (i.e., 2 each for group and phase velocity). These parameters are also unknown in the inversion, and this type of approach is known as hierarchical Bayesian inversion.

Inversion of dispersion curves is a highly nonlinear problem, and analytical computation of PPD is not possible for the nonlinear problem. Additionally, the number of layers is not known in advance, and estimated parameter uncertainties depend on the model complexity. If we add the model complexity, the fit between observed data and synthetic prediction significantly improves but may not be necessarily required by the data. As a result, uncertainties can be large. In contrast, a simple model can predict only some portion of the data, resulting in unrealistically small uncertainties. Here a reversible jump Markov Chain Monte Carlo (rjMCMC) sampling is used to estimate the PPD (Dettmer & Dosso, 2012; Pachhai et al., 2015). In this approach, the model parameters are updated in three different moves: birth, death, and perturbation. In the birth move, a new interface is introduced in a randomly chosen layer, and model parameters (thickness and S-wave velocity) are perturbed from one of the randomly selected layers. In the death move, a layer is randomly picked and subject to deletion (death) with the perturbation of layer thickness and velocity from a randomly selected layer. In the case of the perturbation move, layers are neither introduced nor deleted, but only model parameters are perturbed from a randomly selected layer. All the moves are accepted or rejected based on the Metropolis-Hasting acceptance or rejection criterion (Hastings, 1970; Metropolis et al., 1953) defined by,

$$\alpha = \left(1, \frac{p(\boldsymbol{m}\prime)}{p(\boldsymbol{m})} \frac{L(\boldsymbol{m}\prime)}{L(\boldsymbol{m})} \frac{q(\boldsymbol{m}|\boldsymbol{m}\prime)}{q(\boldsymbol{m}'|\boldsymbol{m})}\right), \tag{5}$$

where $\frac{p(\boldsymbol{m}\prime)}{p(\boldsymbol{m})}$ is the prior ratio and $\frac{q(\boldsymbol{m}|\boldsymbol{m}\prime)}{q(\boldsymbol{m}'|\boldsymbol{m})}$ is the ratio of proposal. The prior and proposal ratios become unity as the prior is fixed in all the iterations and we use a symmetrical distribution for the proposal. The only remaining term in Eq. 5 is the likelihood ratio, and likelihood is computed is computed using Eq. 4.

For a nonlinear problem, the rjMCMC can be very inefficient if low probability regions separate multiple high probability regions. As a result, the sampling needs a long time to converge to the true model. Thus, interacting Markov chains are used here to achieve faster convergence. In this case the acceptance or rejection probability becomes,

$$\alpha = \left(1, \left(\frac{L(m\prime)}{L(m)}\right)^{d\beta}\right), \tag{6}$$

where $d\beta$ represents the tempering parameter (between 0 and 1) which scales the likelihood. For more details of this approach, we refer to Dettmer et al., (2012), Pachhai et al., (2015), and Pachhai et al., (2014).

3.3 Autocorrelation of P-wave coda

The autocorrelation, mathematically, measures the similarity between a timeseries and its delayed version. The autocorrelation method has been a very effective tool in identifying interfaces with a strong impedance contrast in the crust (Gorbatov et al., 2013; Kennett et al., 2015), particularly for shallow crustal structures using teleseismic coda waves (Pham & Tkalcic, 2017, 2018) and ambient noise (Gorbatov et al., 2013). The autocorrelation of a seismic waveform contains many positive and negative peaks. These peaks represent the reverberations of a seismic wave within a layer. Figure S3 illustrates a simple concept of how the autocorrelation method works. In this example, a P-wave incident on a layer with the thickness (H = 3 km), P-wave velocity (Vp = 3.9 km/s), and S-wave velocity (Vs = 1.9 km/s). The incident P wave converts to either P or S at the interface and reverberates within the layer before recording on a seismic recording station (Figure S3a). The impulsive responses of various conversions and reverberation of the incident P-wave are shown in Figure S3b, and their autocorrelations are shown in Figure S3c. The impulses of P-wave reverberation are recorded on the vertical component while both P and S reverberations are recorded on the radial component. Therefore, the vertical and radial seismograms include all the ground motions of the P wave. The autocorrelation produces a symmetrical signal on two sides with the largest amplitude in the center. Therefore, only the positive side is considered after removing the largest amplitude in the center (Figure S3c). The prominent negative amplitude in the autocorrelation of the vertical component is represented by 2p. In this example, it represents the time difference between the reflected phase 3p (this phase is called a reflected phase because it has one reflection on the surface) and transmitted phase 1p. This can be expressed in the following mathematical form.

$$\Delta t_{2p} = t_{3p} - t_{1p} = 2H\sqrt{\frac{1}{V_p^2} - \beta^2}, \tag{7}$$

where β is the ray parameter, H is the layer thickness or depth of the discontinuity in the case of a layer over half-space. For teleseismic earthquakes used in this study, the ray parameter is very small, and square of it is negligible. As a result, Eq. 7 becomes simple velocity formula in which the wave travels the distance 2H. Therefore, the expression for 2p delay time becomes,

$$\Delta t_{2p} = \frac{2H}{V_p}\,. \tag{8}$$

Similarly, the largest negative amplitude in the autocorrelation of the radial component is represented by 2s. In this example, it represents the time difference between the pair of the reverberation 1p2s and transmitted phase 1p. In this case, the expression for the computation of 2s delay time becomes,

$$\Delta t_{2s} = \frac{2H}{V_s}\,, \tag{9}$$

Using these autocorrelation approach, we first measure the delay times of the prominent peaks from the stacked vertical and radial autocorrelograms. We then estimate the layer thickness using P-wave velocity, S-wave velocity, and delay times in Eqs. 8 and 9. Here we utilized the 1-D velocity model derived using joint Bayesian inversion of group and phase velocity dispersions to estimate the depth of the discontinuities.

4. Feasibility study using synthetic data

Before we apply our methods to the observed data, we perform various synthetic tests to illustrate the feasibility of our methods presented in Section 3. In particular, we experiment for the lateral and vertical resolution of our data.

4.1 Lateral resolution

In the first test, we experiment to address the question of lateral resolution of the ambient noise data recorded by stations in Nepal. To determine the lateral resolution (or grid size), we performed checkerboard tests at various periods, using the station distribution considered in this study, applying FMST method (Rawlinson & Sambridge, 2003). We also computed resolution maps using tomographic inversion (Yanovskaya & Ditmar, 1990) applied in this study. More details of the checkerboard test and model resolution are presented in the supplementary material (Text S1-S2).

Results for the checkerboard tests and resolution map are shown in Figures S4-S6. These tests show that 0.30^{o} anomaly size (i.e., 0.15 ^{o} grid size) is well recovered beneath Central Nepal, particularly in the rupture area of the 2015 Gorkha earthquake, at periods 7-20 s (Figure S5). Additionally, the resolution maps (Figure S6) show that our data can resolve as short as 15-km length, particularly in Central Nepal for periods up to 25 s. The resolution length for 35 s is low as we have a limited number of stations for that period. Therefore, we consider 0.30^{o} grid size to compute the group and phase velocity maps for a period range of 3 to 35 s.

4.2 Vertical resolution applying Bayesian inversion

In the second experiment, we test the vertical resolution of S-wave velocity by applying Bayesian inversion of dispersion curves. As the data are weakly sensitive to P-wave velocity and density, we do not invert those parameters. For this test, we prepared synthetic dispersion curves for both phase and group velocity using the Raydisp subroutine (Doornbos, 1988) for various models, which include (1) a weak low velocity in the crust at 10.5 km depth using dispersions for periods 3 to 35 s, (2) same as (1) but using dispersions for periods 5 to 35 s, (3) a strong low velocity in the crust around 30-km depth beneath the surface, (4) velocity increasing as a function of depth. The details of these experiments are mentioned in supplementary materials (Text S3)

These four synthetic experiments suggest that the S-wave velocity is well recovered with narrower uncertainty at a shallower depth, but the uncertainties become larger for deeper depths and at depths where the velocity jump is significant. Additionally, when the lower period data is missing, the resolving power of the data for the shallow crustal structure decreases, thereby increasing the uncertainties. However, when we combine both phase and group velocity dispersions, uncertainties become lower.

4.3 Vertical resolution applying autocorrelation

Here, we present three synthetic experiments for the feasibility of P-wave coda autocorrelation of distant earthquakes to recover the discontinuities in the crust and the Moho depth. In the first experiment, we computed vertical and radial synthetic seismograms (for various epicentral distances) for a 2-layer crustal model with a discontinuity at 8 km depth. Here we computed an impulse response using the respknt code (Randall, 1989), and the impulsive response was convolved with the source (Ricker wavelet). Then the random noise with a 10% standard deviation was added to the synthetic data. Then we computed the autocorrelation of both vertical and radial components. To compute the autocorrelation, we first performed a Fast Fourier transformation (FFT) of the P-wave coda. Then we applied spectral whitening in the frequency domain to enhance the higher-frequency content. The spectral whitened spectrum is obtained by dividing the amplitude spectrum by smoothened average of the spectrum (Pham & Tkalcic, 2017). Finally, we computed the autocorrelation of spectrally whitened data in the frequency domain, and an autocorrelogram in the time domain is obtained by applying the Inverse Fast Fourier Transform (IFFT). Note that the autocorrelation of the whitened signal is band-pass filtered (as described in Section 2) to improve the sharpness of the reflected phases and to avoid the spurious effect caused by the unexpected amplification of very high-frequency noise due to spectral whitening. To enhance the SNR of the signals and suppress the incoherent features such as the effect of the source-time functions, earthquake depth phases, and source side scattering, we stacked the autocorrelation from all the events at various epicentral distances by using phase weighted stacking method (Schimmel & Paulssen, 1997). The results of the synthetic experiments are presented in supplementary materials (Text S4).

All the experiments presented in supplementary materials (see Figure S11-S13) show that the methods described in Section 3 successfully retrieve both lateral and depth structures, including depth discontinuities for different scenarios that have been observed in our study region. We now apply these approaches to the observed data.

5. Results

Figure 4 shows the results for 2-D tomographic maps obtained applying linearized inversion of dispersion curves computed for all the station pairs. The group velocity maps at shorter periods, 5 and 10 s (Figures 5a-b), show the presence of a low-velocity structure south of

MCT. In contrast, high velocities are observed north of the MCT and extend northward to the IYS, which delineates this high-velocity anomaly from a low-velocity anomaly north of the IYS. The low-velocity anomaly observed in the south likely corresponds to sediments believed to have been deposited due to the erosion of Churia Hills and Mahabharat ranges brought by rivers and weathering. We associate the observed high-velocity anomaly between the MCT and IYS with the presence of dense metamorphic rocks of the Higher Himalayan Crystallines (Hodges, 2000; Murphy & Yin, 2003).

At 15 s period, (Figure 4c), we observe a discontinuous high-velocity anomaly between MBT and MCT which broadens and become somewhat continuous at 20 and 30 s (Figures 5d-e). At 35 s period, (Figure 4f), this somewhat continuous high-velocity anomaly breaks into 2 patches of high-velocity zones, with the highest velocities observed beneath Kathmandu. This high-velocity feature maybe associated with the Indian lower crust and upper mantle structure. We also observe low-velocity anomaly north of IYS on the 5 s (Figure 4a) period group map and north of MCT on the 30 and 35 s period maps (Figure 4e-f). This strong low-velocity feature at the higher periods likely indicates that we are sampling upper-mid crustal structures of the thick Tibetan crust.

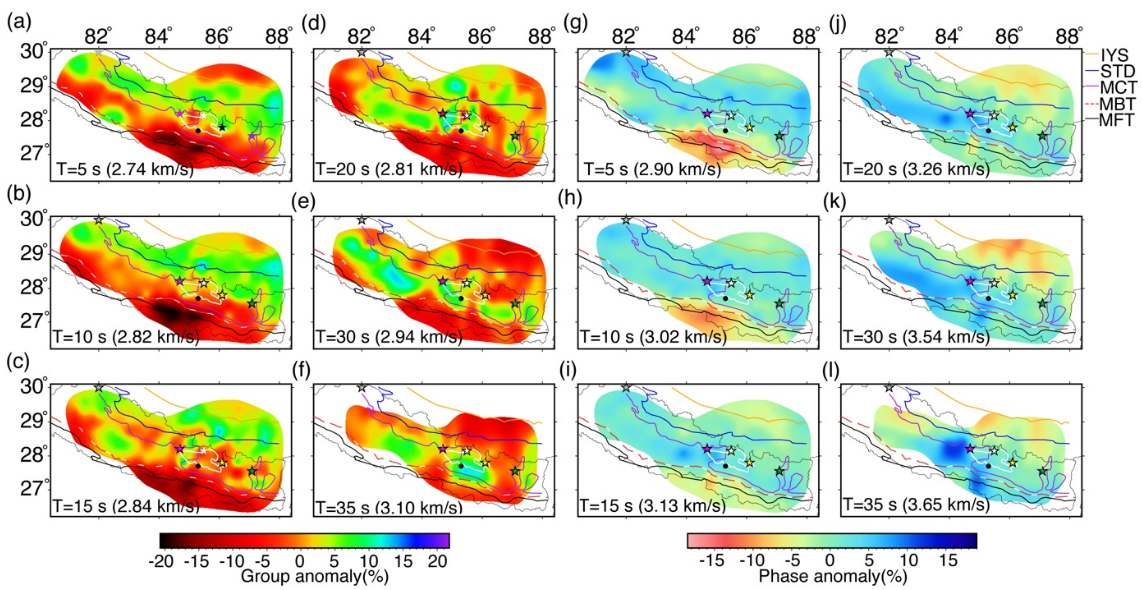

Figure 4. 2-D Rayleigh wave (a-f) group and (g-l) phase velocity anomalies for 5 to 35 s. Period and mean velocity are mentioned at the bottom left corner of each subplot. All the major thrust faults are indicated by lines with different colors. The white line in each subplot indicates the rupture area of the 2015 Gorkha earthquake. Stars with pink and yellow colors

represent the mainshock and the biggest aftershock of the 2015 Gorkha earthquake, while those with grey, white, and green colors represent the 1505, 1833, and 1934 earthquakes, respectively.

Our phase velocity maps (Figure 4g-l), in general, show similar anomaly patterns as observed in the group velocity maps (Figure 4a-f), but here, the anomaly signature can be more easily associated with vertical tectonic structures. For example, the phase velocity maps show a low-velocity anomaly south of our study area at 5 and 10 s period, shutting down at 15 s period (Figure 4g-i). This is in agreement with the presence of a 10 km thick sedimentary basin (Mitra et al., 2006). Also, from 20 to 35 s period (Figure 4j-l), we observe that low velocities are well confined to the north of STD, which is possible due to the thicker crust beneath Tibet.

We then estimated the 1-D S-wave velocity and its uncertainty as a function of depth up to 60 km by applying joint inversion of phase and group dispersions extracted at every node of $0.30^{o} \times 0.30^{o}$ grids. As described in Section 4 for synthetic experiments, Vp/Vs ratio is fixed at 1.73. The P-wave velocity was derived using the Vp/Vs ratio while the density was derived from P-wave velocity. Then we applied our algorithm to estimate the 1-D velocity profiles for S-wave velocity. We then combined all the 1-D velocity profiles to compute the 3-D velocity maps. The uncertainties are computed in the same way, but the 1-standard deviation of the velocity as a function of depth was used. The horizontal slices of 2-D S-wave velocity models at various depths are shown in Figure 5, and their uncertainties are presented in Figure S14.

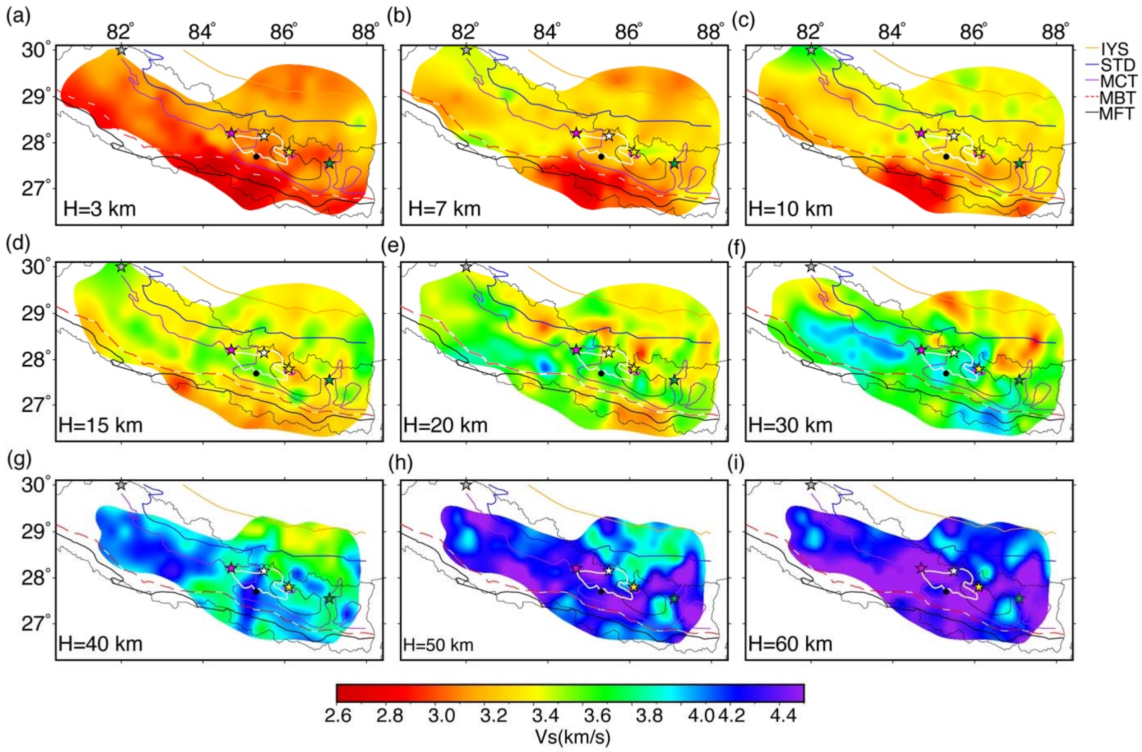

Figure 5. Absolute S-wave velocity at various depths, which are mentioned at the bottom left corner of each subplot. All the major thrust faults are indicated by lines with different colors. The white line in each subplot indicates the rupture area of the 2015 Gorkha earthquake. Stars with pink and yellow colors represent the mainshock and the biggest aftershock of the 2015 Gorkha earthquake, while those with grey, white, and green colors represent the 1505, 1833, and 1934 earthquakes, respectively.

Figure 5 indicates a wider variation of S-wave velocity in shallow crust and uniform in deeper sections. We observed the low S-wave velocity in the south of MBT and the relatively high S-wave velocity in the north of MBT at shallower depths (Figure 5a-c). The low velocity in the south of MBT was also observed by Mitra et al. (2006). The S-wave velocity structure reverses at 20 km depth (Figure 5e), showing low velocity beneath South Tibet and relatively high velocity beneath Nepal. At 20-30 km depth (Figure 5e-f), we observe relatively high S-wave velocity in the region between MCT and STD, which indicates a stronger middle crust beneath Nepal. The same result was obtained by Bai et al. (2019) in their P-wave velocity model. At a depth of 40-50 km (Figure 5g-h), relatively low S-wave velocity is observed beneath South Tibet and high velocity beneath Nepal. However, it is challenging to interpret results at greater depths due to large uncertainties (Figure S14). We found uncertainties increase as a function of depth due to poor sensitivity of dispersions curves (up to 35s) to deeper structures. We also observe higher uncertainties at shallower depths where velocity jumps are strong because the dispersion curves are not sensitive to the depth discontinuities.

We created seven depth profiles of S-wave velocity perpendicular to the strike and two depth profiles of S-wave velocity parallel to the strike of the 2015 Gorkha earthquake, and among them, four profiles are presented in Figure 6, and the other profiles are presented in Figure S15. Figure 6 shows a variation in upper and mid-crustal complexity beneath Nepal and South Tibet. The boundary (black dashed line in Figure 6a-b) that separates the low velocity from high velocity in the south of the duplex (marked as R1, Figure 6a-b) and the boundary that separates high velocity from low velocity in the north of duplex region is considered as the MHT (Priestley et al., 2019). The MHT we consider here is taken from Mencin et al. (2016) and Mendoza et al. (2019). Here, the most pronounced feature is the presence of low velocity up to 10 km in southern Nepal (feature L1, Figure 6a, b, and d) and mid-crustal quasi horizontal LVZ observed between ~15 and 25 km depth along the profiles AA' and BB' (feature L2, Figure 6a and b). Traversing along these profiles, the LVZ is seen to be connected to a shallow and much broader low-velocity region to the south and a deeper prominent sub-horizontal LVZ to the north (feature L3, Figure 6a and b). The presence of a continuous low-velocity layer extending from shallow depths to mid-crustal depths has been observed in receiver function studies beneath Himalaya-Tibet (e.g., Duputel et al., 2016; Nábělek et al., 2009) and has been interpreted as the signature of the MHT.

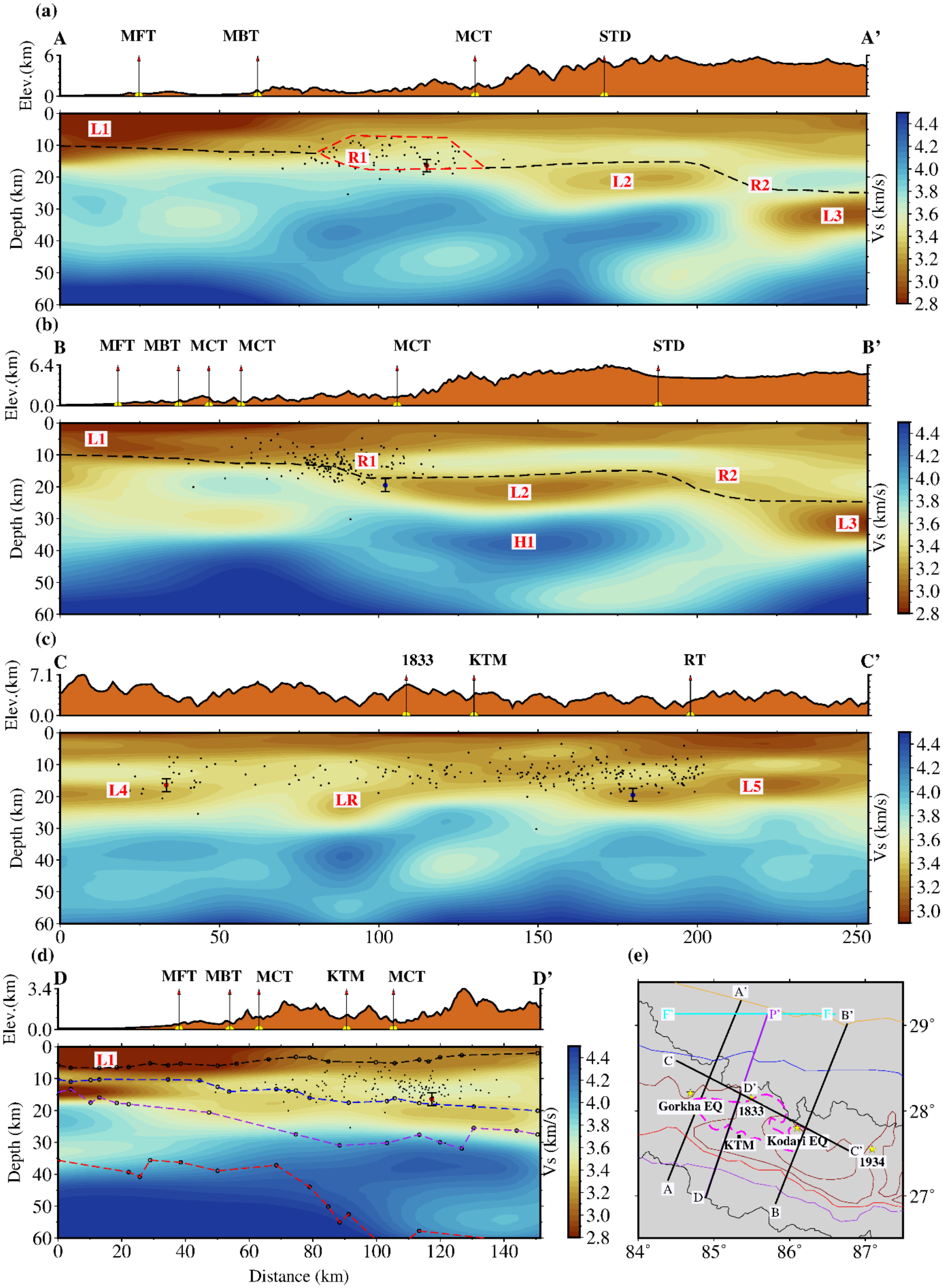

Figure 6. (a-c) S-wave velocity structure as a function of depth along AA', BB', and CC' as shown in (e) with topography on the top. (d) Major interfaces obtained using autocorrelation of P wave coda projected on top of S-wave velocity along DD'. (e) Locations of the profiles

shown in (a-d). Blacked dashed line represents the proposed MHT in this study. Black dots represent the relocated aftershocks (Bai et al., 2016) of the 2015 Gorkha Earthquake. Red dashed line in (a) represents the duplex structure in MHT.

We observed a west-dipping low-velocity structure between the mainshock and the biggest aftershocks of the 2015 Gorkha earthquake on the profile CC' (Figure 6c). This might be the lateral ramp on the MHT as discussed by Kumar et al., (2017) (feature LR, Figure 6c). The profile CC' shows relatively low-velocity anomalies in the west of the mainshock and east of the biggest aftershock of the 2015 Gorkha earthquake (feature L4 and L5, Figure 6c). The high-velocity structures were observed at a depth greater than 30 km due to the subducting Indian crust, but the uncertainties are large at these depths due to strong velocity variation (Figure S16c).

We also found a high S-wave velocity (~4.2 km /s) at depth of 35-40 km beneath the High Himalaya along the profile BB' (feature H1, Figure 6b) with higher uncertainties due to sharp velocity jump (Figure S16b). This high velocity has been previously observed beneath the same region (Guo et al., 2009) as well as beneath India (e.g., Kumar et al., 2021). Monsalve et al. (2008) also found a high Vp/Vs ratio (~1.78) at this depth beneath the High Himalaya while the P-wave velocity is ~7.0 km/s. This gives us an S-wave velocity of ~4.0 km/s which is within the uncertainty of our velocity model. This fast S-wave velocity can be due to the eclogitization of the lower crust (Christensen & Mooney, 1995; Schulte-Pelkum et al., 2005). This could also be due to the underthrusting of the Indian plate (Monsalve et al., 2008).

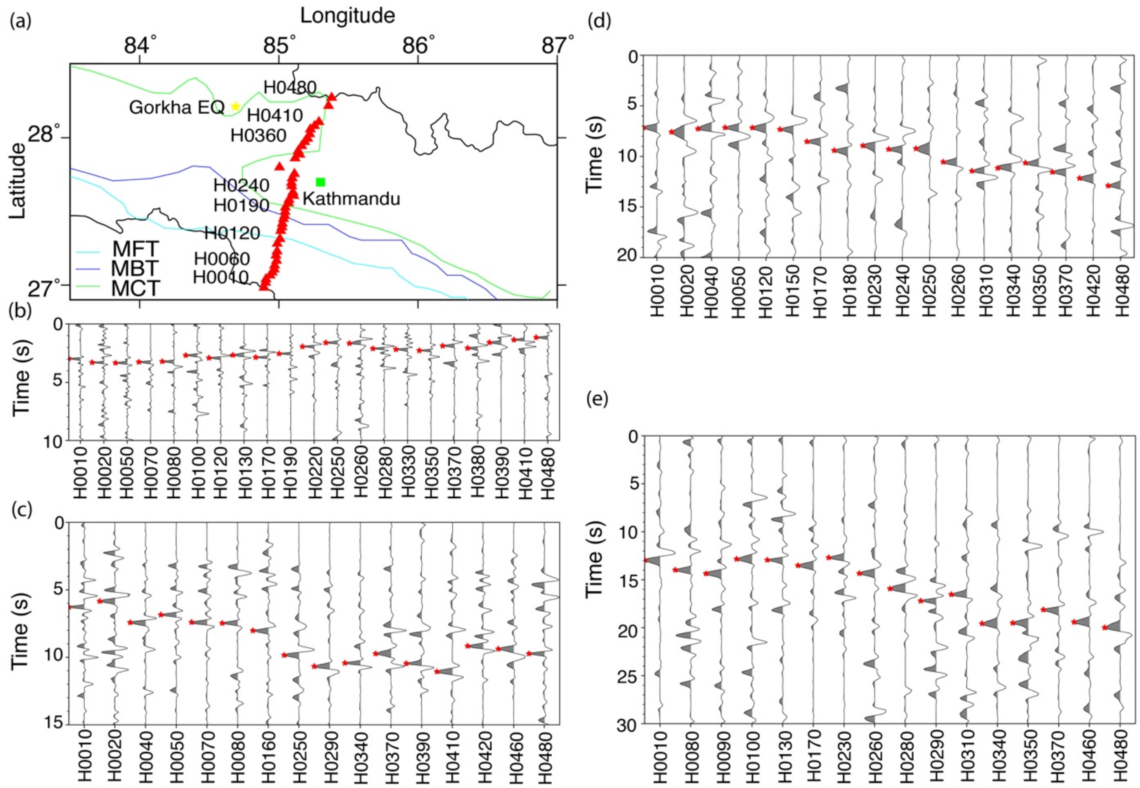

Figure 7. Vertical and radial autocorrelation stacks for different seismic stations along South-North in Central Nepal. The red star shows the prominent phases in the autocorrelogram which indicate the time picks of P reflections. (a) Station distribution map used in autocorrelation. (b) Delay time of the 2p phase corresponding to shallow interface. (c) Delay time of the 2s phase corresponding to the MHT. (d) Delay time of the 2p phase corresponding to the interface between upper and lower Indian crust. (e) Delay time of the 2p phase corresponding to the Moho.

In addition to the velocity model, we estimated seismic interfaces from autocorrelation. We used the velocity model obtained from our work to convert the delay time to depth information and overlaid the results on the velocity model along the DD' profile located in the vicinity of the HiCLIMB stations (Figure 6d). Results for individual stations stacked autocorrelations are presented in Figure 7. The depth interfaces computed beneath all the stations are overlaid on the S-wave velocity profile in Figure 6d and they are separately presented in Figure S17. We identify four interfaces beneath our study region. The depth of interface by using our S-wave velocity model beneath each station is presented in Figure S17. The depth of the top interface decreases towards the north (Figure 7b and Figure S17), which is well correlated with the geology of Nepal (Upreti, 1999). The southern portion may represent the sediments deposited beneath Nepal. The depth of the second interface is 10 km in the southern part and increases to 20 km in the north (Figure 7d and Figure S17). This interface follows the transition from a high-velocity layer to a lower velocity and may represent the MHT. The third interface is located at the transition from low velocity to high velocity with a depth of 20 km in the south and 30 km in the north (Figure 7c and Figure S17), and this discontinuity may represent an interface between the upper and lower Indian crust. The fourth interface is located at a depth of 40 km beneath the southern and deepens north of MCT (Figure 7e and Figure S17). We interpret this as the Moho beneath the region. Previous studies also show a similar Moho depth in the region (e.g., Hetényi et al., 2006; Nábělek et al., 2009; Schulte-Pelkum et al., 2005).

6. Discussion

To provide a high-resolution velocity structure of the lithosphere and geometries of discontinuities beneath Nepal Himalaya, we performed a joint analysis of ambient noise tomography and autocorrelation of coda P waveforms using data from different networks of seismic stations located in Nepal and India.

The determination of the 3-D S-wave velocity model is from the inversion of the Rayleigh wave group and phase velocities derived from ambient noise cross-correlation. The inversion results indicate a pronounced LVZ at 15-25 km depth (feature L2, Figure 6a-b). The presence of a LVZ beneath Nepal Himalaya has been reported in previous studies along different receiver function profiles (e.g., Duputel et al., 2016; Nábělek et al., 2009) but our results provide an absolute 3-D S-wave velocity structure. This LVZ is interpreted as the signature of the MHT.

To the south, the LVZ is connected to a broader shallower low-velocity region, where most seismicity is confined. This shallow low-velocity region appears to be connected to the LVZ through a ramp structure (feature R1, Figure 6a and b). The location of low velocity at this ramp has been identified as duplex using the aftershocks density of the 2015 Gorkha earthquake (Mendoza et al., 2019) where a system of multiple north-dipping faults is bounded. We cannot identify all the dipping faults in this ramp due to the resolution length being longer than the width of the duplex zone, but all the faults shown by aftershocks are within a ramp of this broad low velocity. The low velocity inside the duplex structure is expected due to multiple faults within a system.

CMT analysis of the Gorkha main shock and Mw > 5.0 aftershocks by Duputel et al. (2016) have shown that the flat portion of MHT is located within the shallow low-velocity region observed in our model and also seen on receiver function analysis. The geometry of the MHT has been outlined as a ramp-flat-ramp with shallow thrust fault flattening at depths between 10 and 15 km followed by a mid-crustal ramp connecting to a deeper low-dipping thrust at depths greater than 25 km (Duputel et al., 2016). Our models indicate that the LVZ (feature L2, Figure 7a-b) seen by Duputel et al. (2016) as a deeper LVZ is connected to a much deeper LVZ (feature L3, Figure7a-b) through another ramp (feature R2, Figure 7a-b). This suggests that the MHT that was previously described as a continuous low-velocity structure (Nábělek et al., 2009) corresponds most likely to a system of LVZ connected by ramps. The presence of mid-crustal ramps beneath Lesser Himalaya affects the interseismic period as well as coseismic rupture segmentation and rupture characteristics (Dal Zilio et al., 2021). Also, it has a great implication for the Himalayan seismic cycle as well as the long-term construction of the Himalayas (Dal Zilio et al., 2021).

The LVZ (feature L2, Figure 6a-b) we observed appears to resist the hypocenter location from migrating towards north. It appears that although the shallow portion of the MHT can host seismicity, the deeper LVZ may be creeping and/or ductile and may indicate the presence of aqueous fluids at high pore pressure. This low velocity also correlates well with high electrical conductivity (Unsworth et al., 2005) and low Vp/Vs ratio in the region (Monsalve et al., 2008). Additionally, high attenuation for the S and P waves has been observed in this region (Sheehan et al., 2014).

During the interseismic period, MHT can stably creep in the LVZ and locked south of it. This might result from the interseismic stress build-up in the border between the locked and continuously creeping part of the MHT (Bilham et al., 2017; Mencin et al., 2016). High shear stress rate was reported by Ader et al. (2012) in the south of the LVZ.

The low velocity (feature L3, Figure 6a-b) in the middle crust (~25-30 km) observed beneath South Tibet is consistent with previous studies (Nelson et al., 1996; Schulte-Pelkum et al., 2005; Unsworth et al., 2005; Zhao et al., 1993). This low velocity may indicate the presence of mechanically weak crust beneath South Tibet, which plays a significant role in Himalaya-Tibetan orogenic processes. Based on the thermal structure and composition of the rocks, partial melting seems to occur within the crust beneath South Tibet (McKenna & Walker, 1990). Shear heating along the plate boundary may warm the upper crust beneath South Tibet and the temperature line to cross to the melt line of the materials which is supported by thermal structure across our study region (Henry et al., 1997; Nelson et al., 1996; Royden, 1993; Wang et al., 2013). Thus, the low mid-crustal velocity observed in our study beneath south Tibet may be an indication of the presence of partial melt. Moreover, the low-velocity reservoir beneath the High Himalaya and South Tibet (Figure 6a-b and Figure S15) might be compatible with an electrically highly conductive zone revealed by the magnetotelluric study across our study region (Lemonnier et al., 1999).

To understand whether the low S-wave velocity we observe at the MHT depth is real (Figure 6b), we performed a synthetic experiment. In this experiment, synthetic dispersion curves were computed for the BB' profile (Figure 6b). Then the noise described in Section 4 was added to all the synthetic data. We then considered these synthetic dispersion curves with noise as data in the inversion. Figure 8 shows the comparison of the true velocity model (Figure 8a) and the retrieved velocity model (Figure 8b). This comparison shows that the slow S-wave velocity layers are well retrieved along the BB' profile with narrow uncertainties up to the depth of 40 km beneath the surface (Figure 8c). The uncertainties increase as a function of depth due to the weaker sensitivity of the dispersions data to the deeper structure. We also observe higher uncertainties at layer interface positions because the inversion tries to retrieve discontinuity through velocity smearing by adding layers. This experiment suggests that the observed low velocities are not an artifact of the inversion procedure.

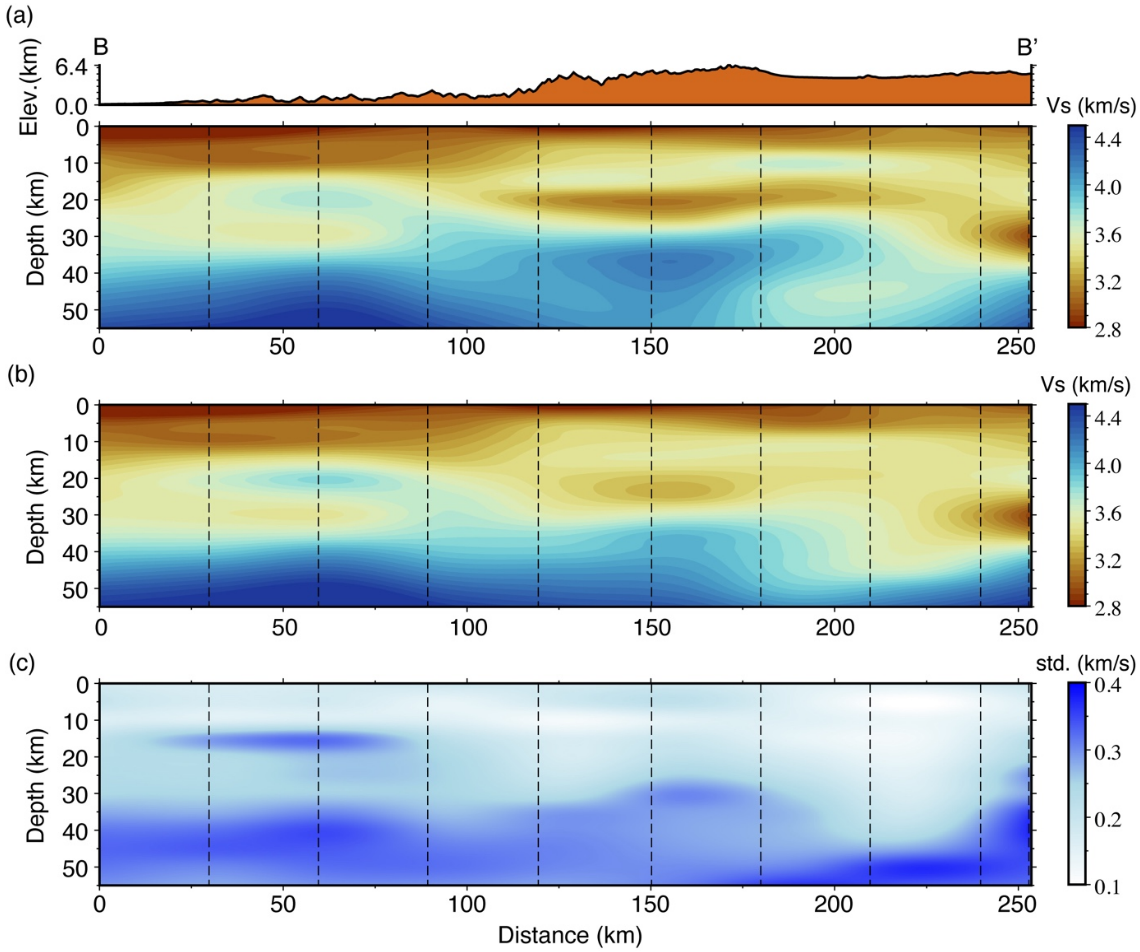

Figure 8. (a) True velocity model along profile BB' used to produce synthetic group and phase dispersion curves. (b) Velocity model recovered from non-linear Bayesian inversion. (c) Uncertainty corresponding to the inverted velocity model shown in (b).

We also extract the lateral variation of S-velocity across the MHT (Figure 9). The MHT depth was picked based on the MHT discontinuity suggested by the autocorrelation of coda waves. Figure 9 shows that the 2015 Gorkha earthquake nucleated in the high S-wave velocity region. Another high-velocity patch is observed around the hypocenter of the biggest aftershocks where the seismic density map before the biggest aftershock shows a higher density of aftershocks (Baillard et al., 2017). The boundary between high and relatively low velocity (North of Kathmandu) is the region, where Pandey et al. (1999) observed significantly different seismicity. The marked difference in velocity between the west and east is observed in the region where the rupture of the mainshock terminates. This low velocity is well observed in our north-south profile as well (feature L3, Figures 7a-b).

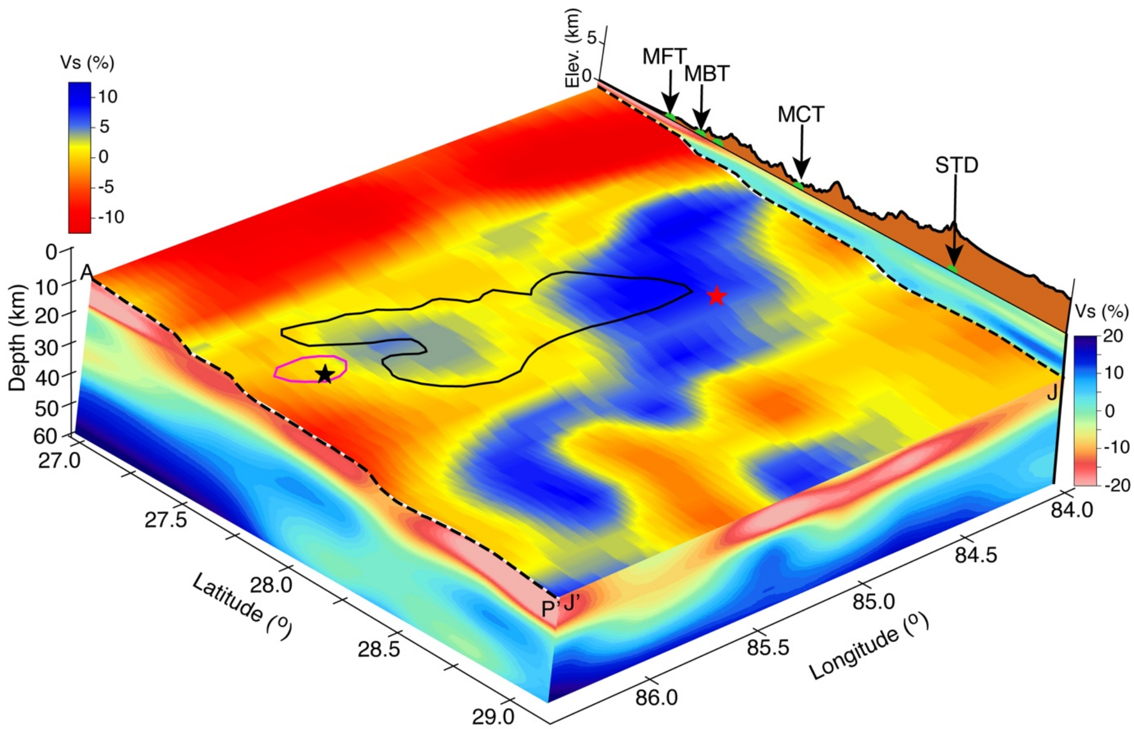

Figure 9. Lateral variation of S-wave velocity anomaly across the MHT surface (from mean = 3.35 km/s) extracted using autocorrelation of coda P waves, and S-wave velocity anomaly as a function of depth (from mean velocity=3.80 km/s) along south-north (AP' in Figure 6e) and west-east (J'J in Figure 6e) direction. The black and magenta solid line on the MHT represents the rupture of the Mainshock (red star) and the biggest aftershock (black star) of the 2015 Gorkha earthquake, respectively.

The lateral variation of S-wave velocity in the MHT is due to a change in the elastic properties of the material. The high S-wave velocity obtained in the west of longitude ~86° and low velocity in the east of it indicates the presence of different elastic properties of the rock in this area. The lateral variation of S-wave velocity across MHT further provides details across the rupture area. The presence of an up-dip ramp towards the south and a downdip ramp towards the north of the coseismic rupture of the 2015 Gorkha earthquake might have played a crucial role in controlling the rupture in both directions (e.g., Avouac et al., 2015; Duputel et al., 2016; Wang et al., 2017), while the rupture arrested in the east may be explained by the presence of slow velocity material there (Figure 9). The high velocity observed around the hypocenter of the 2015 Gorkha earthquake indicates the presence of highly rigid material there, which is favorable for the nucleation of an earthquake. The relatively low-velocity region between the two high-velocity patches may also be the lateral ramp on the MHT (Kumar et al., 2017). The presence of a relatively low-velocity region beneath the north of Kathmandu may have slowed down the rupture velocity of the 2015 Gorkha mainshock and increased again in the region having a high-velocity patch (Harris & Day, 1997), observed near the hypocenter of the biggest aftershock, then finally arrested in the low-velocity region at longitude ~86°.

The observed high and relatively low velocities agree with the P wave structure estimated within the rupture area (Pei et al., 2016). Previous studies show that the slip and energy radiated are relatively higher in the region where we observe higher velocity than in the low-velocity region (Fan & Shearer, 2015; Grandin et al., 2015). Baillard et al. (2017) also found a seismic gap in that area, while Hoste-Colomer et al. (2017) proposed a tear fault.

7. Conclusions

We presented a highly resolved 3-D structure of the crust and discontinuities, including the MHT beneath Himalaya Nepal, using ambient noise tomography and autocorrelation of the P-wave coda. This can be used to better understand the earthquakes, their locations, the physics of earthquakes, and mitigation of the seismic hazard in this region. Our results show that the velocity structure and interface depths identified by using autocorrelation agree well such that those discontinuities identified by autocorrelation are in the transitions from either low to high or high to low-velocity structure except for the topmost interface. We found two slow-velocity ramps connected by a flat low-velocity layer sandwiched between high velocities. This low velocity could be due to the aqueous fluid brought by the subduction of the Indian crust. The presence of two ramps on the MHT at different depths has been well supported by both the coseismic and postseismic data of the 2015 Gorkha earthquake. The first ramp beneath the Lesser Himalaya correlates with the duplex structure on the MHT that has been proposed using aftershocks, although we cannot identify all the ramps within a duplex system due to the resolution limit. The second ramp beneath the High Himalayas is connected to a broad low velocity beneath South Tibet which may be due to the partial melt. We also observe a high-velocity structure at ~35-40 km beneath the High Himalayas due to the partial eclogitization in the lower crust.

We show that high resolution ambient noise tomography and autocorrelation of the P-wave coda can illuminate a detailed geometry of the MHT. Our results (Fig. 6a-b) allow us to identify within the overall structure of the MHT a clear LVZ (feature L2, in between two ramps R1 and R2), that is interpreted as the signature and downdip extent of the zone of incomplete seismic coupling (e.g., Bilham, 2019). This zone exhibits different downdip widths along strike. In Central Nepal, where the 2015 Mw 7.8 Gorkha nucleated, the width of the flat coupling zone as inferred from the extent of the LVZ is about 50-70 km while in Eastern Nepal (feature L2 in Figure 6a), close to the source of the 1934 Mw 8.4 earthquake, the width is about 90-100 km (feature L2 in Figure 6b). These estimates are comparable with the downdip width of fault coupling estimated by Lindsey et al., (2018) along similar transects in Nepal using GPS data set. Furthermore, the stored elastic energy prior to an earthquake (e.g., Bilham et al., 2017; Kanamori & Brodsky, 2004) along a 50-70 km and 90-100 km-wide coupling zones satisfies the rupture estimates of the 2015 Mw 7.8 and the 1934 Mw 8.4 events respectively.

The close correspondence of our estimates, both in Central and Eastern Nepal, of the geometry and extent of the L2 LVZ with those of the decollement coupling zone inferred from GPS data, along with the respective slip from individual earthquake ruptures suggest an interesting avenue of research to decipher the paradox of variable surface slip at the front of MHT as retrieved from paleoseismic trenching in the Himalaya (e.g., Kumar et al., 2010; Sapkota et al., 2013; Upreti et al., 2007; Wesnousky et al., 2017). A systematic mapping of L2 LVZ beneath the Himalaya integrating seismic tomography and GPS geodesy can therefore provide a physical and a mechanical understanding of maximum Himalayan earthquake magnitudes (Bilham, 2019; Stevens & Avouac, 2016). The occurrence of millenary Mw>9.0 earthquakes (Stevens & Avouac, 2016) in Central and Eastern Nepal would require either a wider L2 LVZ than the ones identified in this work or the involvement of L3 LVZ identified beneath southern Tibet in storing enough elastic energy (Bilham, 2019; Feldl & Bilham, 2006).

Acknowledgement

H.R. Thapa acknowledges from Generali Insurance Group and The Abdus Salam International Centre for Theoretical Physics (ICTP)" for providing financial support during his PhD studies. We thank Thanh Son Pham for the discussion about autocorrelation. All the computations were performed on the ICTP Argo cluster. We would like to acknowledge UK funding source and the SEIS-UK for the seismic instrumentation for the Cambridge network and Indian Institute of Science Education and Research Kolkata (IISER-K) for providing the data of six seismic stations. We would also like to thank people from Nepal Seismological

Center in Kathmandu and Regional Seismological Center in Surkhet who helped on the deployment, maintenance, and decommissioning of Cambridge network. The facilities of IRIS Data Services, and specifically the IRIS Data Management Center, were used to access waveforms, related metadata, and/or derived products used in this study. IRIS Data Services are funded through the Seismological Facilities for the Advancement of Geoscience and EarthScope (SAGE) Proposal for the National Science Foundation under Cooperative Agreement EAR-1261681.

References

Ader, T., Avouac, J. P., Liu-Zeng, J., Lyon-Caen, H., Bollinger, L., Galetzka, J., et al. (2012). Convergence rate across the Nepal Himalaya and interseismic coupling on the Main Himalayan Thrust: Implications for seismic hazard. *Journal of Geophysical Research: Solid Earth*, *117*(4). https://doi.org/10.1029/2011JB009071

Agrawal, M., Das, M. K., Kumar, S., & Pulliam, J. (2021). Mapping lithospheric seismic structure beneath the Shillong plateau (India) and adjoining regions by jointly fitting receiver functions and surface wave dispersion. *Geophysical Journal International*, *226*(3), 1645–1675. https://doi.org/10.1093/gji/ggab146

Avouac, J.-P. (2007). Dynamic Processes in Extensional and Compressional Settings - Mountain Building: From Earthquakes to Geological Deformation. *Treatise on Geophysics*, *6*, 377–439.

Avouac, J.-P., Meng, L., Wei, S., Wang, T., & Ampuero, J.-P. (2015). Lower edge of locked Main Himalayan Thrust unzipped by the 2015 Gorkha earthquake. *Nature Geoscience*, *8*(9), 708–711.

Backus, G., & Gilbert, F. (1968). The resolving power of gross earth data. *Geophysical Journal International*, *16*(2), 169–205.

Bai, L., Liu, H., Ritsema, J., Mori, J., Zhang, T., Ishikawa, Y., & Li, G. (2016). Faulting structure above the Main Himalayan Thrust as shown by relocated aftershocks of the 2015 Mw7. 8 Gorkha, Nepal, earthquake. *Geophysical Research Letters*, *43*(2), 637–642.

Bai, L., Klemperer, S. L., Mori, J., Karplus, M. S., Ding, L., Liu, H., et al. (2019). Lateral variation of the Main Himalayan Thrust controls the rupture length of the 2015 Gorkha earthquake in Nepal. *Science Advances*, *5*(6), eaav0723.

Baillard, C., Lyon-Caen, H., Bollinger, L., Rietbrock, A., Letort, J., & Adhikari, L. B. (2017). Automatic analysis of the Gorkha earthquake aftershock sequence: evidences of structurally segmented seismicity. *Geophysical Journal International*, *209*(2), 1111–1125. https://doi.org/10.1093/gji/ggx081

Bensen, G. D., Ritzwoller, M. H., Barmin, M. P., Levshin, A. L., Lin, F., Moschetti, M. P., et al. (2007). Processing seismic ambient noise data to obtain reliable broad-band surface wave dispersion measurements. *Geophysical Journal International*, *169*(3), 1239–1260.

Bilham, R. (2019). Himalayan earthquakes: a review of historical seismicity and early 21st century slip potential. *Geological Society, London, Special Publications*, *483*(1), 423–482. https://doi.org/10.1144/SP483.16

Bilham, R., & Wallace, K. (2005). Future Mw>8 Earthquakes in the Himalaya: Implications From the 26 Dec 2004 Mw= 9.0 Earthquake on India’s Eastern Plate Margin. *Geol Surv India Spec Publ*, *85*, 1--14.

Bilham, R., Mencin, D., Bendick, R., & Bürgmann, R. (2017). Implications for elastic energy storage in the Himalaya from the Gorkha 2015 earthquake and other incomplete ruptures of the Main Himalayan Thrust. *Quaternary International*, *462*, 3–21. https://doi.org/10.1016/j.quaint.2016.09.055

Bollinger, L., Avouac, J. P., Beyssac, O., Catlos, E. J., Harrison, T. M., Grove, M., et al. (2004). Thermal structure and exhumation history of the Lesser Himalaya in central Nepal. *Tectonics*, *23*(5), n/a-n/a. https://doi.org/10.1029/2003TC001564

Bollinger, L., Lyon-Caen, H., & RESIF. (2011). HiK-NET temporary experiment (RESIF-SISMOB). RESIF - Réseau Sismologique et géodésique Français. https://doi.org/10.15778/RESIF.ZO2014

Castaldo, R., De Novellis, V., Solaro, G., Pepe, S., Tizzani, P., De Luca, C., et al. (2017). Finite element modelling of the 2015 Gorkha earthquake through the joint exploitation of DInSAR measurements and geologic-structural information. *Tectonophysics*, *714*, 125–132.

Christensen, N. I., & Mooney, W. D. (1995). Seismic velocity structure and composition of the continental crust: A global view. *Journal of Geophysical Research: Solid Earth*, *100*(B6), 9761–9788. https://doi.org/10.1029/95JB00259

Copley, A., Avouac, J.-P., & Royer, J.-Y. (2010). India-Asia collision and the Cenozoic slowdown of the Indian plate: Implications for the forces driving plate motions. *Journal of Geophysical Research: Solid Earth*, *115*(B3).

Dal Zilio, L., Hetényi, G., Hubbard, J., & Bollinger, L. (2021). Building the Himalaya from tectonic to earthquake scales. *Nature Reviews Earth & Environment*, *2*(4), 251–268. https://doi.org/10.1038/s43017-021-00143-1

DeCelles, P. G., Kapp, P., Gehrels, G. E., & Ding, L. (2014). Paleocene-Eocene foreland basin evolution in the Himalaya of southern Tibet and Nepal: Implications for the age of initial India-Asia collision. *Tectonics*, *33*(5), 824–849. https://doi.org/10.1002/2014TC003522

Dettmer, J., & Dosso, S. E. (2012). Trans-dimensional matched-field geoacoustic inversion with hierarchical error models and interacting Markov chains. *The Journal of the Acoustical Society of America*, *132*(4), 2239–2250.

Dettmer, J., Molnar, S., Steininger, G., Dosso, S. E., & Cassidy, J. F. (2012). Trans-dimensional inversion of microtremor array dispersion data with hierarchical autoregressive error models. *Geophysical Journal International*, *188*(2), 719–734.

Dewey, J. F., & Bird, J. M. (1970). Mountain belts and the new global tectonics. *Journal of Geophysical Research*, *75*(14), 2625–2647. https://doi.org/10.1029/JB075i014p02625

Doornbos, D. J. (1988). Multiple scattering by topographic relief with application to the core-mantle boundary. *Geophysical Journal International*, *92*, 465--478. https://doi.org/https://doi.org/10.1111/j.1365-246X.1988.tb00009.x

Duputel, Z., Vergne, J., Rivera, L., Wittlinger, G., Farra, V., & Hetényi, G. (2016). The 2015 Gorkha earthquake: a large event illuminating the Main Himalayan Thrust fault. *Geophysical Research Letters*, *43*(6), 2517–2525.

Dziewonski, A. M., Chou, T.-A., & Woodhouse, J. H. (1981). Determination of earthquake source parameters from waveform data for studies of global and regional seismicity. *Journal of Geophysical Research: Solid Earth*, *86*(B4), 2825–2852. https://doi.org/10.1029/JB086iB04p02825

Ekström, G., Nettles, M., & Dziewoński, A. M. (2012). The global CMT project 2004–2010: Centroid-moment tensors for 13,017 earthquakes. *Physics of the Earth and Planetary Interiors*, *200–201*, 1–9. https://doi.org/10.1016/j.pepi.2012.04.002

Elliott, J. R., Jolivet, R., González, P. J., Avouac, J.-P., Hollingsworth, J., Searle, M. P., & Stevens, V. L. (2016). Himalayan megathrust geometry and relation to topography revealed by the Gorkha earthquake. *Nature Geoscience*, *9*(2), 174–180. https://doi.org/10.1038/ngeo2623

Fan, W., & Shearer, P. M. (2015). Detailed rupture imaging of the 25 April 2015 Nepal earthquake using teleseismic P waves. *Geophysical Research Letters*, *42*(14), 5744–5752. https://doi.org/10.1002/2015GL064587

Feldl, N., & Bilham, R. (2006). Great Himalayan earthquakes and the Tibetan plateau. *Nature*, *444*(7116), 165–170. https://doi.org/10.1038/nature05199

Gansser, A. (1964). Geology of the Himalayas : London. *Wiley Interscience*, 289p.

Gorbatov, A., Saygin, E., & Kennett, B. L. N. (2013). Crustal properties from seismic station autocorrelograms. *Geophysical Journal International*, *192*(2), 861–870.

Grandin, R., Vallée, M., Satriano, C., Lacassin, R., Klinger, Y., Simoes, M., & Bollinger, L. (2015). Rupture process of the M w = 7.9 2015 Gorkha earthquake (Nepal): Insights into Himalayan megathrust segmentation. *Geophysical Research Letters*, *42*(20), 8373–8382. https://doi.org/10.1002/2015GL066044

Guo, Z., Gao, X., Yao, H., Li, J., & Wang, W. (2009). Midcrustal low-velocity layer beneath the central Himalaya and southern Tibet revealed by ambient noise array tomography. *Geochemistry, Geophysics, Geosystems*, *10*(5).

Harris, R. A., & Day, S. M. (1997). Effects of a low-velocity zone on a dynamic rupture. *Bulletin of the Seismological Society of America*, *87*, 1267--1280.

Hastings, W. K. (1970). Monte Carlo sampling methods using Markov chains and their applications. *Biometrika*, *57*(1), 97–109. https://doi.org/10.1093/biomet/57.1.97

Hazarika, D., Hajra, S., Kundu, A., Bankhwal, M., Kumar, N., & Pant, C. C. (2020). Imaging the Moho and Main Himalayan Thrust beneath the Kumaon Himalaya: constraints from receiver function analysis. *Geophysical Journal International*, *224*(2), 858–870. https://doi.org/10.1093/gji/ggaa478

Henry, P., Le Pichon, X., & Goffé, B. (1997). Kinematic, thermal and petrological model of the Himalayas: constraints related to metamorphism within the underthrust Indian crust and topographic elevation. *Tectonophysics*, *273*(1–2), 31–56.

Herman, F., Copeland, P., Avouac, J.-P., Bollinger, L., Mahéo, G., Le Fort, P., et al. (2010). Exhumation, crustal deformation, and thermal structure of the Nepal Himalaya derived from the inversion of thermochronological and thermobarometric data and modeling of the topography. *Journal of Geophysical Research*, *115*(B6), B06407. https://doi.org/10.1029/2008JB006126

Herrmann, R. B. (2013). Computer programs in seismology: An evolving tool for instruction and research. *Seismological Research Letters*, *84*(6), 1081–1088.

Hetényi, G., Cattin, R., Vergne, J., & Nábělek, J. L. (2006). The effective elastic thickness of the India Plate from receiver function imaging, gravity anomalies and thermomechanical modelling. *Geophysical Journal International*, *167*(3), 1106–1118. https://doi.org/10.1111/j.1365-246X.2006.03198.x

Hodges, K. V. (2000). Tectonics of the Himalaya and southern Tibet from two perspectives. *Geological Society of America Bulletin*, *112*(3), 324–350. https://doi.org/10.1130/0016-7606(2000)112<324:TOTHAS>2.0.CO;2

Hoste-Colomer, R., Bollinger, L., Lyon-Caen, H., Burtin, A., & Adhikari, L. B. (2017). Lateral structure variations and transient swarm revealed by seismicity along the Main Himalayan Thrust north of Kathmandu. *Tectonophysics*, *714–715*, 107–116. https://doi.org/10.1016/j.tecto.2016.10.004

Hubbard, J., Almeida, R., Foster, A., Sapkota, S. N., Bürgi, P., & Tapponnier, P. (2016). Structural segmentation controlled the 2015 M w 7.8 Gorkha earthquake rupture in Nepal. *Geology*, *44*(8), 639–642. https://doi.org/10.1130/G38077.1

Kanamori, H., & Brodsky, E. E. (2004). The physics of earthquakes. *Reports on Progress in Physics*, *67*(8), 1429–1496. https://doi.org/10.1088/0034-4885/67/8/R03

Karplus, M. S., Pant, M., Sapkota, S. N., Nábělek, J., Velasco, A. A., Adhikari, L. B., et al. (2020). A Rapid Response Network to Record Aftershocks of the 2015 M 7.8 Gorkha Earthquake in Nepal. *Seismological Research Letters*, *91*(4), 2399–2408. https://doi.org/10.1785/0220190394

Kennett, B. L. N. (2015). Lithosphere--asthenosphere P-wave reflectivity across Australia. *Earth and Planetary Science Letters*, *431*, 225–235.

Kennett, B. L. N., Saygin, E., & Salmon, M. (2015). Stacking autocorrelograms to map Moho depth with high spatial resolution in southeastern Australia. *Geophysical Research Letters*, *42*(18), 7490–7497.

Khanal, S., & Robinson, D. M. (2013). Upper crustal shortening and forward modeling of the Himalayan thrust belt along the Budhi-Gandaki River, central Nepal. *International Journal of Earth Sciences*, *102*(7), 1871–1891. https://doi.org/10.1007/s00531-013-0889-1

Kumar, A., Singh, S. K., Mitra, S., Priestley, K. F., & Dayal, S. (2017). The 2015 April 25 Gorkha (Nepal) earthquake and its aftershocks: implications for lateral heterogeneity on the Main Himalayan Thrust. *Geophysical Journal International*, *208*(2), 992–1008. https://doi.org/10.1093/gji/ggw438

Kumar, A., Kumar, N., Mukhopadhyay, S., & Klemperer, S. L. (2021). Tomographic Image of Shear Wave Structure of NE India Based on Analysis of Rayleigh Wave Data. *Frontiers in Earth Science*, *9*. https://doi.org/10.3389/feart.2021.680361

Kumar, N., Aoudia, A., Guidarelli, M., Babu, V. G., Hazarika, D., & Yadav, D. K. (2019). Delineation of lithosphere structure and characterization of the Moho geometry under the Himalaya–Karakoram–Tibet collision zone using surface-wave tomography. *Geological Society, London, Special Publications*, *481*(1), 19–40. https://doi.org/10.1144/SP481-2017-172

Kumar, S., Wesnousky, S. G., Rockwell, T. K., Ragona, D., Thakur, V. C., & Seitz, G. G. (2001). Earthquake Recurrence and Rupture Dynamics of Himalayan Frontal Thrust, India. *Science*, *294*(5550), 2328–2331. https://doi.org/10.1126/science.1066195

Kumar, S., Wesnousky, S. G., Rockwell, T. K., Briggs, R. W., Thakur, V. C., & Jayangondaperumal, R. (2006). Paleoseismic evidence of great surface rupture earthquakes along the Indian Himalaya. *Journal of Geophysical Research: Solid Earth*, *111*(B3), n/a-n/a. https://doi.org/10.1029/2004JB003309

Kumar, S., Wesnousky, S. G., Jayangondaperumal, R., Nakata, T., Kumahara, Y., & Singh, V. (2010). Paleoseismological evidence of surface faulting along the northeastern Himalayan front, India: Timing, size, and spatial extent of great earthquakes. *Journal of Geophysical Research*, *115*(B12), B12422. https://doi.org/10.1029/2009JB006789

Lavé, J., & Avouac, J.-P. (2000). Active folding of fluvial terraces across the Siwaliks Hills, Himalayas of central Nepal. *Journal of Geophysical Research: Solid Earth*, *105*(B3), 5735–5770.

Lemonnier, C., Marquis, G., Perrier, F., Avouac, J.-P., Chitrakar, G., Kafle, B., et al. (1999). Electrical structure of the Himalaya of central Nepal: High conductivity around the mid-crustal ramp along the MHT. *Geophysical Research Letters*, *26*(21), 3261–3264. https://doi.org/10.1029/1999GL008363

Lindsey, E. O., Almeida, R., Mallick, R., Hubbard, J., Bradley, K., Tsang, L. L. H., et al. (2018). Structural Control on Downdip Locking Extent of the Himalayan Megathrust. *Journal of Geophysical Research: Solid Earth*, *123*(6), 5265–5278. https://doi.org/10.1029/2018JB015868

MacKay, D. J. C. (2003). *Information Theory, Inference, and Learning Algorithms*. Retrieved from https://www.bibsonomy.org/bibtex/24c23fea472f6e75c0964badd83883d77/tmalsburg

Manu-Marfo, D., Aoudia, A., Pachhai, S., & Kherchouche, R. (2019). 3D shear wave velocity model of the crust and uppermost mantle beneath the Tyrrhenian basin and margins. *Scientific Reports*, *9*(1), 3609. https://doi.org/10.1038/s41598-019-40510-z

McKenna, L. W., & Walker, J. D. (1990). Geochemistry of crustally derived leucocratic igneous rocks from the Ulugh Muztagh area, northern Tibet and their implications for the formation of the Tibetan Plateau. *Journal of Geophysical Research: Solid Earth*, *95*(B13), 21483–21502.

Meigs, A. J., Burbank, D. W., & Beck, R. A. (1995). Middle-late Miocene (>10 Ma) formation of the Main Boundary thrust in the western Himalaya. *Geology*, *23*(5), 423. https://doi.org/10.1130/0091-7613(1995)023<0423:MLMMFO>2.3.CO;2

Mencin, D., Bendick, R., Upreti, B. N., Adhikari, D. P., Gajurel, A. P., Bhattarai, R. R., et al. (2016). Himalayan strain reservoir inferred from limited afterslip following the Gorkha earthquake. *Nature Geoscience*, *9*(7), 533–537. https://doi.org/10.1038/ngeo2734

Mendoza, M. M., Ghosh, A., Karplus, M. S., Klemperer, S. L., Sapkota, S. N., Adhikari, L. B., & Velasco, A. (2019). Duplex in the Main Himalayan Thrust illuminated by aftershocks of the 2015 Mw 7.8 Gorkha earthquake. *Nature Geoscience*, *12*(12), 1018–1022. https://doi.org/10.1038/s41561-019-0474-8

Metropolis, N., Rosenbluth, A. W., Rosenbluth, M. N., Teller, A. H., & Teller, E. (1953). Equation of State Calculations by Fast Computing Machines. *The Journal of Chemical Physics*, *21*(6), 1087–1092. https://doi.org/10.1063/1.1699114

Mitra, S., Priestley, K., Gaur, V. K., Rai, S. S., & Haines, J. (2006). Variation of Rayleigh wave group velocity dispersion and seismic heterogeneity of the Indian crust and uppermost mantle. *Geophysical Journal International*, *164*(1), 88–98.

Mohammadi, N., Rahimi, H., Gholami, A., Pachhai, S., & Aoudia, A. (2022). Shear-wave velocity structure of upper mantle along the Zagros collision zone. *Tectonophysics*, *837*, 229444. https://doi.org/10.1016/j.tecto.2022.229444

Molnar, P. (1984). Structure and tectonics of the Himalaya: Constraints and implications of geophysical data. *Annual Review of Earth and Planetary Sciences*, *12*(1), 489–516.

Molnar, P., & Tapponnier, P. (1975). Cenozoic Tectonics of Asia: Effects of a Continental Collision: Features of recent continental tectonics in Asia can be interpreted as results of the India-Eurasia collision. *Science*, *189*(4201), 419–426. https://doi.org/10.1126/science.189.4201.419

Monsalve, G., Sheehan, A., Rowe, C., & Rajaure, S. (2008). Seismic structure of the crust and the upper mantle beneath the Himalayas: Evidence for eclogitization of lower crustal rocks in the Indian Plate. *Journal of Geophysical Research: Solid Earth*, *113*(B8).

Mosegaard, K., & Tarantola, A. (1995). Monte Carlo sampling of solutions to inverse problems. *Journal of Geophysical Research: Solid Earth*, *100*(B7), 12431–12447. https://doi.org/10.1029/94JB03097

Murphy, M. A., & Yin, A. (2003). Structural evolution and sequence of thrusting in the Tethyan fold-thrust belt and Indus-Yalu suture zone, southwest Tibet. *Geological Society of America Bulletin*, *115*(1), 21–34.

Nabelek, J. (2002). Collaborative Research: Lithospheric Scale Dynamics of Active Mountain Building along the Himalayan-Tibetan Collision Zone. International Federation of Digital Seismograph Networks. https://doi.org/10.7914/SN/XF_2002

Nábělek, J., Hetényi, G., Vergne, J., Sapkota, S., Kafle, B., Jiang, M., et al. (2009). Underplating in the Himalaya-Tibet collision zone revealed by the Hi-CLIMB experiment. *Science*, *325*(5946), 1371–1374.

Nelson, K. D., Zhao, W., Brown, L. D., Kuo, J., Che, J., Liu, X., et al. (1996). Partially molten middle crust beneath southern Tibet: synthesis of project INDEPTH results. *Science*, *274*(5293), 1684–1688.

Pachhai, S., Tkalčić, H., & Dettmer, J. (2014). Bayesian inference for ultralow velocity zones in the Earth's lowermost mantle: complex ULVZ beneath the east of the Philippines. *Journal of Geophysical Research: Solid Earth*, *119*(11), 8346–8365.

Pachhai, S., Dettmer, J., & Tkalčić, H. (2015). Ultra-low velocity zones beneath the Philippine and Tasman Seas revealed by a trans-dimensional Bayesian waveform inversion. *Geophysical Journal International*, *203*(2), 1302–1318.

Pachhai, S., Li, M., Thorne, M. S., Dettmer, J., & Tkalčić, H. (2022). Internal structure of ultralow-velocity zones consistent with origin from a basal magma ocean. *Nature Geoscience*, *15*(1), 79–84. https://doi.org/10.1038/s41561-021-00871-5

Pandey, M. ., Tandukar, R. ., Avouac, J. ., Vergne, J., & Héritier, T. (1999). Seismotectonics of the Nepal Himalaya from a local seismic network. *Journal of Asian Earth Sciences*, *17*(5–6), 703–712. https://doi.org/10.1016/S1367-9120(99)00034-6

Pandey, M. R., Tandukar, R. P., Avouac, J. P., Lave, J., & Massot, J. P. (1995). Interseismic strain accumulation on the Himalayan crustal ramp (Nepal). *Geophysical Research Letters*, *22*(7), 751–754.

Pearson, O. N. (2002). *Structural evolution of the central Nepal fold-thrust belt and regional tectonic and structural significance of the Ramgarh thrust*. The University of Arizona.

Pearson, O. N., & DeCelles, P. G. (2005). Structural geology and regional tectonic significance of the Ramgarh thrust, Himalayan fold-thrust belt of Nepal. *Tectonics*, *24*(4), n/a-n/a. https://doi.org/10.1029/2003TC001617

Pei, S., Liu, H., Bai, L., Liu, Y., & Sun, Q. (2016). High-resolution seismic tomography of the 2015 M w 7.8 Gorkha earthquake, Nepal: Evidence for the crustal tearing of the Himalayan rift. *Geophysical Research Letters*, *43*(17), 9045–9052. https://doi.org/10.1002/2016GL069808

Pham, T. S., & Tkalcic, H. (2017). On the feasibility and use of teleseismic P wave coda autocorrelation for mapping shallow seismic discontinuities. *Journal of Geophysical Research: Solid Earth*, *122*(5), 3776–3791.

Pham, T. S., & Tkalcic, H. (2018). Antarctic ice properties revealed from teleseismic P wave coda autocorrelation. *Journal of Geophysical Research: Solid Earth*, *123*(9), 7896–7912.

Priestley, K., Ho, T., & Mitra, S. (2019). The crustal structure of the Himalaya: A synthesis. *Geological Society, London, Special Publications*, *483*(1), 483–516. https://doi.org/10.1144/SP483-2018-127

Randall, G. E. (1989). Efficient calculation of differential seismograms for lithospheric receiver functions. *Geophysical Journal International*, *99*(3), 469–481.

Rawlinson, N., & Sambridge, M. (2003). SEISMIC TRAVELTIME TOMOGRAPHY OF THE CRUST AND LITHOSPHERE (pp. 81–198). https://doi.org/10.1016/S0065-2687(03)46002-0

Royden, L. H. (1993). The steady state thermal structure of eroding orogenic belts and accretionary prisms. *Journal of Geophysical Research: Solid Earth*, *98*(B3), 4487–4507.

Ruigrok, E., & Wapenaar, K. (2012). Global-phase seismic interferometry unveils P-wave reflectivity below the Himalayas and Tibet. *Geophysical Research Letters*, *39*(11).

Sapkota, S. N., Bollinger, L., Klinger, Y., Tapponnier, P., Gaudemer, Y., & Tiwari, D. (2013). Primary surface ruptures of the great Himalayan earthquakes in 1934 and 1255. *Nature Geoscience*, *6*(1), 71–76.

Schimmel, M., & Paulssen, H. (1997). Noise reduction and detection of weak, coherent signals through phase-weighted stacks. *Geophysical Journal International*, *130*(2), 497–505.

Schulte-Pelkum, V., Monsalve, G., Sheehan, A., Pandey, M. R., Sapkota, S., Bilham, R., & Wu, F. (2005). Imaging the Indian subcontinent beneath the Himalaya. *Nature*, *435*(7046), 1222–1225.

Searle, M. P., Windley, B. F., Coward, M. P., Cooper, D. J. W., Rex, A. J., Rex, D., et al. (1987). The closing of Tethys and the tectonics of the Himalaya. *Geological Society of America Bulletin*, *98*(6), 678. https://doi.org/10.1130/0016-7606(1987)98<678:TCOTAT>2.0.CO;2

Seeber, L., & Armbruster, J. G. (1981). Great detachment earthquakes along the Himalayan arc and long- term forecasting. In *Earthquake prediction: an international review* (pp. 259–277). https://doi.org/10.1029/me004p0259

Sheehan, A. (2001). Himalayan Seismotectonics, Nepal and Tibet. International Federation of Digital Seismograph Networks. https://doi.org/10.7914/SN/YL_2001

Sheehan, A. F., de la Torre, T. L., Monsalve, G., Abers, G. A., & Hacker, B. R. (2014). Physical state of Himalayan crust and uppermost mantle: Constraints from seismic attenuation and velocity tomography. *Journal of Geophysical Research: Solid Earth*, *119*(1), 567–580.

Stevens, V. L., & Avouac, J. -P. (2016). Millenary M w > 9.0 earthquakes required by geodetic strain in the Himalaya. *Geophysical Research Letters*, *43*(3), 1118–1123. https://doi.org/10.1002/2015GL067336

Stevens, V. L., & Avouac, J. P. (2015). Interseismic coupling on the main Himalayan thrust.

Geophysical Research Letters, *42*(14), 5828–5837. https://doi.org/10.1002/2015GL064845

Subedi, S., Hetényi, G., Vergne, J., Bollinger, L., Lyon-Caen, H., Farra, V., et al. (2018). Imaging the Moho and the Main Himalayan Thrust in Western Nepal With Receiver Functions. *Geophysical Research Letters*, *45*(24). https://doi.org/10.1029/2018GL080911

Tapponnier, P., Peltzer, G., Le Dain, A. Y., Armijo, R., & Cobbold, P. (1982). Propagating extrusion tectonics in Asia: New insights from simple experiments with plasticine. *Geology*, *10*(12), 611. https://doi.org/10.1130/0091-7613(1982)10<611:PETIAN>2.0.CO;2

Unsworth, M. J., Jones, A. G., Wei, W., Marquis, G., Gokarn, S. G., & Spratt, J. E. (2005). Crustal rheology of the Himalaya and Southern Tibet inferred from magnetotelluric data. *Nature*, *438*(7064), 78–81.

Upreti, B. N. (1999). An overview of the stratigraphy and tectonics of the Nepal Himalaya. *Journal of Asian Earth Sciences*, *17*(5–6), 577–606.

Upreti, B. N., Kumahara, Y., & Nakata, T. (2007). Paleoseismological study in the Nepal Himalaya-present status. In *Proceedings of the Korea-Nepal Joint symposium on slope stability and landslides* (pp. 1--9).

Wang, C., Chen, W.-P., & Wang, L.-P. (2013). Temperature beneath Tibet. *Earth and Planetary Science Letters*, *375*, 326–337. https://doi.org/10.1016/j.epsl.2013.05.052

Wang, X., Wei, S., & Wu, W. (2017). Double-ramp on the Main Himalayan Thrust revealed by broadband waveform modeling of the 2015 Gorkha earthquake sequence. *Earth and Planetary Science Letters*, *473*, 83–93. https://doi.org/10.1016/j.epsl.2017.05.032

Wei, Y., Zhang, S., Li, M., Wu, T., Hua, Y., Zhang, Y., & Cai, J. (2021). Regional lithospheric deformation beneath the East Qinling-Dabie orogenic belt based on ambient noise tomography. *Geophysical Journal International*. https://doi.org/10.1093/gji/ggab393

Wesnousky, S. G., Kumar, S., Mohindra, R., & Thakur, V. C. (1999). Uplift and convergence along the Himalayan Frontal Thrust of India. *Tectonics*, *18*(6), 967–976.

https://doi.org/10.1029/1999TC900026

Wesnousky, S. G., Kumahara, Y., Chamlagain, D., Pierce, I. K., Reedy, T., Angster, S. J., & Giri, B. (2017). Large paleoearthquake timing and displacement near Damak in eastern Nepal on the Himalayan Frontal Thrust. *Geophysical Research Letters*, *44*(16), 8219–8226. https://doi.org/10.1002/2017GL074270

Wesnousky, S. G., Kumahara, Y., Nakata, T., Chamlagain, D., & Neupane, P. (2018). New Observations Disagree With Previous Interpretations of Surface Rupture Along the Himalayan Frontal Thrust During the Great 1934 Bihar-Nepal Earthquake. *Geophysical Research Letters*, *45*(6), 2652–2658. https://doi.org/10.1002/2018GL077035

Wobus, C., Heimsath, A., Whipple, K., & Hodges, K. (2005). Active out-of-sequence thrust faulting in the central Nepalese Himalaya. *Nature*, *434*(7036), 1008–1011. https://doi.org/10.1038/nature03499

Wu, S., Yao, J., Wei, S., Hubbard, J., Wang, Y., Min Htwe, Y. M., et al. (2021). New insights into the structural heterogeneity and geodynamics of the Indo-Burma subduction zone from ambient noise tomography. *Earth and Planetary Science Letters*, *562*, 116856. https://doi.org/10.1016/j.epsl.2021.116856

Xu, Z. J., Song, X., & Zhu, L. (2013). Crustal and uppermost mantle S velocity structure under Hi-CLIMB seismic array in central Tibetan Plateau from joint inversion of surface wave dispersion and receiver function data. *Tectonophysics*, *584*, 209–220.

Yanovskaya, T. B., & Ditmar, P. G. (1990). Smoothness criteria in surface wave tomography. *Geophysical Journal International*, *102*(1), 63–72.

Zhao, W., Nelson, K. D., Che, J., Quo, J., Lu, D., Wu, C., & Liu, X. (1993). Deep seismic reflection evidence for continental underthrusting beneath southern Tibet. *Nature*, *366*(6455), 557–559.